HEAT TRANSFER IN SELECTIVE LASER SINTERING OF POLYAMIDE POWDERS

Balaji Soundararajan

UNIVERSITY OF SALERNO

DEPARTMENT OF INDUSTRIAL ENGINEERING

Ph.D. Course in Industrial Engineering
Curriculum in Chemical Engineering - XXXIII Cycle

HEAT TRANSFER IN SELECTIVE LASER SINTERING OF POLYAMIDE POWDERS

Supervisors
Prof. Massimo Poletto
Prof. Diego Barletta
Dr Daniele Sofia

Ph.D. student
Balaji Soundararajan

Scientific Referees
Prof. Rossella Girimonte
Dr Francesco Miccio

Ph.D. Course Coordinator
Prof. Francesco Donsi

Acknowledgments

I am greatly indebted to my supervisors, Prof. Massimo Poletto, Prof. Diego Barletta and Dr. Daniele Sofia for giving me the opportunity to undertake my PhD thesis at the Department of Industrial engineering, University of Salerno. They have been of continuous support, especially during the tough times in the last three years, be it technical or administrative support. The project would not have been possible without their guidance. I would like to extend my gratitude to my supervisor at Airbus central research and technology in Munich, Dr. Elmar Bonaccurso for hosting me. I thank the European Union's Multi scale thermomechanical behaviour of granular materials (Mathegram) consortium (Project number 813202) for the fellowship to carry out the project. Special thanks to my colleagues at the Powder technology laboratory for their support during the course of my work. Last but not the least, I would like to thank my family for their continuous support.

Salerno, 2024 Balaji Soundararajan

Publications

- Balaji Soundararajan, Daniele Sofia, Diego Barletta, Massimo Poletto, *Mesoscale modelling and experimental validation of heat transfer in single-layer selective laser sintering of polyamide powders (Submitted)*

- Balaji Soundararajan, Daniele Sofia, Diego Barletta, Massimo Poletto, *Review on modelling techniques for powder bed fusion processes based on physical principles*, Additive Manufacturing, Volume 47, 2021, 102336, ISSN 2214-8604

- B. Soundararajan, D. Sofia, D. Barletta, M. Poletto, *The set Up of an Experimental Testing Rig to Measure Time and Space Temperature Profiles in Laser Sintering of Polymeric Powders*, Chemical Engineering Transactions, *86*, 781-786, 2021.

Conferences

- Experimental and mesoscale modelling of process parameters in SLS of PA12 powder, Partec conference, Nuremberg, Sept 2023

- Thermal effects and heat transfer in powder layer generation and sintering in the SLS process, CFDEM conference, Graz, April 2023

- Heat transfer modelling and in-situ experimental validation of single-layer selective laser sintering of polyamide powders, World congress in Particle technology, WCPT 9, Madrid, Sept 2022

- Heat transfer in polymeric powders with application to selective laser sintering and powder coating : similarities and challenges : UK particle technology forum, May 2022

- In-situ monitoring and modelling of single-layer selective laser sintering of polyamide powders, International Conference on Conveying and Handling of Particulate Solids (CHoPS), Salerno, July 2022

- The Setup of an experimental testing rig to measure time and space temperature profiles in Laser Sintering of Polymeric powders: International Conference on Chemical and Process Engineering (ICheap-15) Virtual International conference, 23-26 May 2021, Naples, Italy

Table of Contents

List of figures

List of tables

List of symbols

Symbol	Parameter	Units
B	Spectral radiance	$W.Sr^{-1}.m^{-2}Hz^{-1}$
H	Planck's constant	$J.Hz^{-1}$
c	Speed of light	ms^{-1}
λ	Wavelength	nm
K	Temperature	Kelvin
k	Thermal conductivity	$W(m.K)^{-1}$
Hz	Frame rate	Hertz
T	Time	s
ZnSe	Zinc selenide	-
Q	Heat input	W
ε	Emissivity	-
A	Absorptivity	m^{-1}
T	Temperature	K
T_0	Ambient temperature	K
ρ	Density	$Kg(m)^{-3}$
Cp	Specific heat	$J(Kg.K)^{-1}$
H	Enthalpy	J
I	Laser intensity	$W(m)^{-2}$

r	Radius of laser	m^2
ω	Radius of intensity drop	m^2
k_{eff}	Effective thermal conductivity	$W(m.K)^{-1}$
k_s	Thermal conductivity of solid	$W(m.K)^{-1}$
k_{liquid}	Thermal conductivity of liquid	$W(m.K)^{-1}$
k_g	Thermal conductivity of gas	$W(m.K)^{-1}$
D	Diameter of particle	m^2
d	Diameter of carbon black	m^2
h	Convective heat transfer co-efficient	$W(m)^{-2}(K)^{-1}$
σ	Stefan Boltzmann's constant	$W(m)^{-2}(K)^{-4}$
S	Surface are	m^2
F	View factor	-

Abstract

Selective Laser Sintering (SLS) is a type of Laser Powder bed fusion (LPBF) and is a layer-wise Additive Manufacturing (AM) process, with which a complex geometry can be manufactured using granular materials. The complex laser-material interaction and the knowledge of associated process parameters is a challenge in the modelling of the SLS process which in turn helps in the standardization of the process. The knowledge of the temperature field in the powder bed is vital in understanding the powder binding mechanism. One of the major defects of the SLS produced parts is the delamination between the layers which is due to lack of fusion. In this study, a stationary laser sintering experimental set-up equipped with two infrared cameras is built to measure the temperature distribution along the depth and the top surface. A thin layer of polymeric powder is spread on infrared-transparent Zinc Selenide (ZnSe) glass so one of the thermal cameras can see the heat transfer along the depth from the bottom. A carbon black treated polyamide 12 (PA12 CB) powder of average particle size distribution of 60µm and PA6 CB of average particle size distribution of 80µm are used in this study. The experiments were conducted by heating the sample for 10 s and allowing it to cool down. A three-dimensional finite element model considering conductive, convective, radiative heat transfer and phase change is developed to accompany the experimental data. As a first, a temperature-dependent emissivity is considered in the model. A statistical examination using the Design of Experiments (DoE) method was performed to evaluate the uncertain material properties such as thermal conductivity and laser absorptivity and their effect on the time-dependent temperature evolution in the powder bed. The accuracy of the model is validated by comparing the temperature data along xyz directions with the experimental values. The PA6 CB powder exhibits higher laser absorption and higher thermal conductivity than PA12 CB. This is evident from the rapid heating of PA6 CB due to higher laser absorption and faster cooling rate due to higher thermal conductivity. The emissivity of the powder bed is nearly uniform with temperature for both powders and drastically increases at melt pool. This change in emissivity is captured in the model. As an add on to the project, heat transfer in electrostatic powder coating is studied. A Finite elements based model is developed with infrared heat input model. The model helps in understanding the temperature reached during infrared heating and subsequently, to know the ideal power required for the heater.

Keywords: Infrared thermography, finite element methods, heat transfer, temperature history.

Introduction and aim of the work

Multiscale Analysis of Thermo-mechanical Behaviour of Granular Materials (Mathegram) is intended to promote a collaborative research focused on the thermo-mechanical analysis of granular materials. Granular materials are ubiquitous, and their applications are in a wide variety of industries.

In the manufacturing industry, the usage of granular materials in Additive Manufacturing (AM) of products using Laser based powder bed fusion (L-PBF) technique has garnered special interest all over the world due to its ability to manufacture very complex parts at relatively lower costs compared to conventional Subtractive Manufacturing techniques. The parts are built by sintering or melting layer by layer, and the design freedom and part optimization strategies offered by this process is ideal for high-value, low-volume manufacturing industries such as aerospace, automotive and medical (Pereira et al., 2019). Although there are lot of advantages in using this process, Quality Assurance (QA) of the components produced by the AM process seems to be a major challenge (Esfahani et al., 2019). Despite continuous technological advancements in the field of AM, the lack of process repeatability and stability represents a barrier to the industrial breakthrough. The most relevant metal/ceramics-based AM applications currently involve industrial sectors (e.g. aerospace and biomedical) where defects avoidance is of utmost importance (Grasso & Colosimo, 2017a). This creates a need for a deeper understanding of the types of defects during/after an AM process, especially the L-PBF process based on Laser Sintering/Melting. Section 2 will summarize the scientific objectives of the apparatus that has been built, the working principle of SLS and the types of defects in the parts manufactured using L-PBF process. In order to detect these defects during the building process and to keep the process under stable control on a layer-by-layer basis, process monitoring methodologies based on in-situ sensing devices are absolutely necessary. It is also vital to understand the heat transfer during the L-PBF process within the powder bed and with the environment. A thermography-based infra-red visualization technique is well suited for this purpose and is being adopted. Section 3 describes basics of IR thermography, state-of-the-art thermography techniques in LPBF, experiment building and experimental results. Section 4 discusses the state-of-the-art numerical modelling, introduction to the finite-element-based model and results. Section 5 briefs about the heat transfer in powder coating and the similarities with LPBF process.

The primary objectives of the work are as follows:

- To build an infrared thermography-based experimental setup to visualize the thermal changes in the powder bed during L-PBF process using an infra-red camera positioned above the laser hitting point in order to estimate local conductive, radiative and convective heat transfer and contemporarily observing the formation of the melt pool to estimate heat sinks to latent heat.
- To conduct experiments with the thermal camera positioned below the powder bed to visualize the laser penetration on the powder bed and thermal profile, thereby identifying the effectiveness of the vertical conduction and laser penetration process and eventually to evaluate the sensitive material and process parameters suitable for SLS.
- Both the above-mentioned experiments will be used to calibrate and validate the numerical heat transfer model solved by means of COMSOL software, based on Finite element methods (FEM).
- To apply similar heat transfer methodology in the different applications of heat transfer in electrostatic powder coating study.

Chapter I
Selective Laser Sintering

I.1 Selective Laser Sintering: Working principle

Selective Laser Sintering is a subset of the Laser powder bed fusion (L-PBF) process in which any complex geometry is manufactured layer by layer with the laser as a heat source. Firstly, the Computer Aided Design (CAD) file of the part that is to be printed is converted into Stereolithography format (STL) and is fed into the Laser scanning mechanism of the L-PBF machine. A powder spreading mechanism prepares the powder bed by spreading the powder into the build platform. Each layer is typically in the micrometric range, and the laser scans through the layer, thereby sintering/melting the particles and fusing them. Once the layer is sintered or melted as per the part dimensions, the powder spreading mechanism prepares the powder bed for the next layer to be fused. Figure I.0.1 shows the basic working principle of L-PBF process. Two major types of L-PBF processes are the Selective Laser Sintering (SLS) and the Selective Laser Melting (SLM) (Sofia et al., 2015). The Laser power used to melt the particles in SLM is higher than in SLS (Kruth et al., 2005). Due to the fact the particles are not completely melted during SLS process thereby the temperatures involved are slightly lower than in SLM, and the overall artefact shrinkage is lesser. This makes SLS process more interesting than SLM for producing precision components such as porous scaffolds in biomedical applications (Zhou et al., 2008). Our project focuses on the SLS form of the L-PBF process.

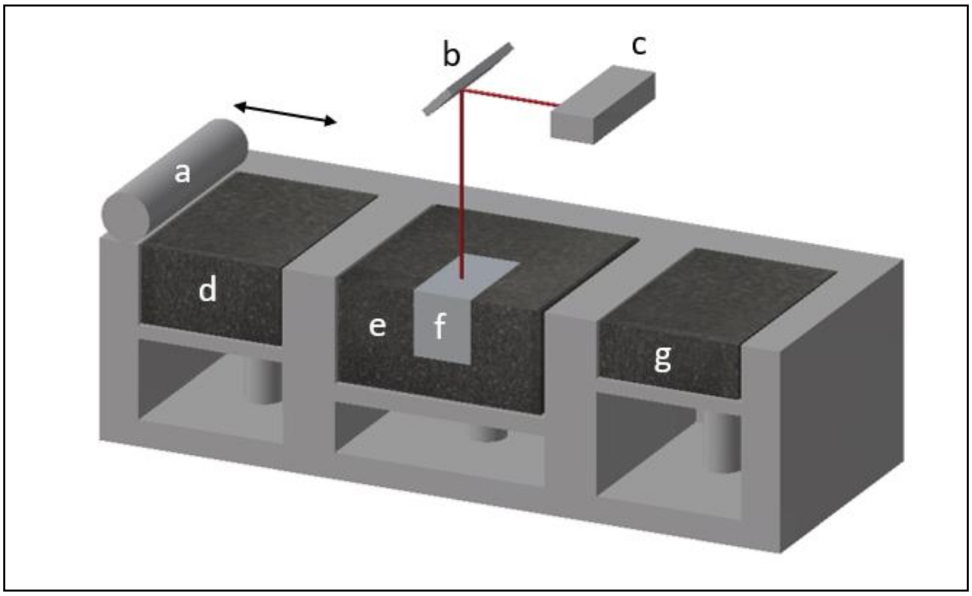

Figure I.0.1 Working of a Laser based Powder bed fusion process (a) roller (b) Laser scan system (c) Laser source (d) Input powder reservoir (e) building chamber (f) specimen (g) reservoir (Soundararajan et al., 2021)

As sketched in Figure I.0.1, the part is built layer by layer, and each part may contain hundreds and thousands of layers fused together. The Laser scanning system deflects and builds the part over two-dimensional area in XY plane, whereas the build platform moves in the vertical Z direction. The parts produced often need to be post-processed for removal of excess powder, or surface finishing may also be required. The advantages of the SLS/SLM process include: 1) the design freedom, the ability to build unconventional and complex parts, which can be used extensively in the area of topology optimization. 2) since laser is used as the energy source, due to its precision, parts with high resolutions can be manufactured. 3) the raw material wastages are reduced and unused powders can be recycled. However, care has to be taken as not a wide range of materials can be readily used in the SLS/SLM process. The LPBF parts are not used widespread across industries due to limited repeatability of the process and to inherent issues and defects of the parts. The issues with the parts manufactured with SLS/SLSM are discussed in the following section.

I.2 Types of defects in LPBF

The parts manufactured by the LPBF processes have various defects due to complex phenomena such as: laser absorption and heat generation, thermal gradients, phase changes from powder to melting pool formation to evaporation and solidification, Marangoni convection due to surface tension gradients which are not fully understood (Bauereiß et al., 2014). Due to these reasons, parts made by LPBF tend to have poor thermo-mechanical properties and standardization in the industries is difficult due to this. The following section describes the types of defects:

Balling: Material droplet (ball) formation, also known as balling, occurs when the molten material solidifies into spheres instead of solid layers, which is a serious hindrance to interlayer connection (Kruth et al., 2004). Figure I.0.2 shows the balling phenomena at different scan speeds (R. Li et al., 2012). Surface tension drives the balling effect by preventing the molten material from wetting the underlying layer. The resulting surface is rough and bead-shaped one that produces an irregular layer deposition with a detrimental effect on the density and quality of the part. (R. Li et al., 2012) discussed three detrimental effects of the balling phenomenon in PBF process: (1) it can increase the surface roughness; (2) a large number of pores can be formed between the discontinuous metallic balls; (3) in case of very severe balling, the spheres protruding from the powder layer may interfere with the movement of the powder deposition system.

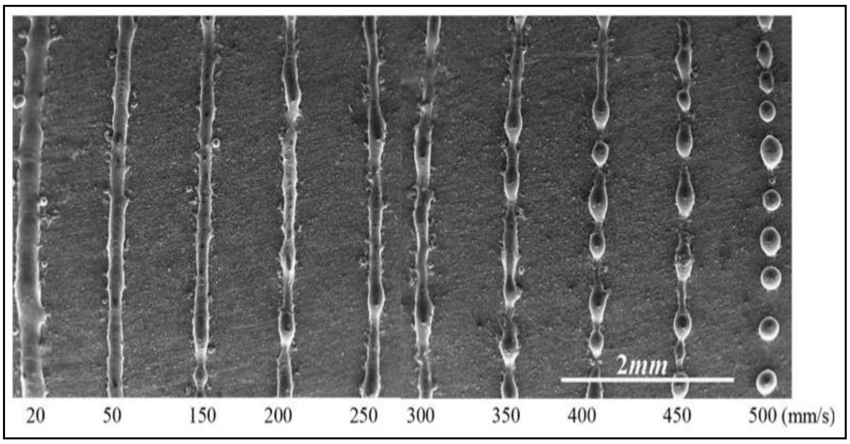

Figure I.0.2 SEM image of balling effect at different Laser scan speeds (R. Li et al., 2012)

Porosity: Porosity is a critical parameter in an L-PBF process as it strongly impacts the fatigue performances, crack growth and propagation of AM parts (Edwards et al., 2013). Much work investigating the porosity in PBF process has been done (Slotwinski et al., 2014). These voids can be found (1) within a layer (2) between adjacent layers (3) on the external surface of the part. Most common pores are found within the layer. Also, the pores can be of different shapes and sizes. The voids observed between the layers are called acicular pores (Smith et al., 2016) and are characterized by elongated shapes. Figure I.0.3 shows the SEM images of pores (Tammas-Williams et al., 2015). Pores found on the external surface are usually referred to as surface porosity.

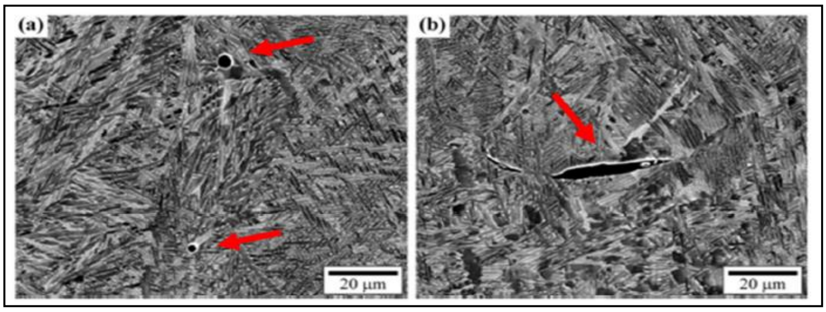

Figure I.0.3 SEM images of Pores: (a) spherical pores (b) elongated or acicular pores (Tammas-Williams et al., 2015)

Residual stresses, cracking and de-lamination: Residual stresses in the L-PBF process have been pointed out to arise from two different mechanisms: (1) thermal gradient mechanism and (2) cool down phase of molten top layers. A repeated heating and cooling cycle occurs during the process, giving rise to residual stresses due to different local thermal deformation. Cracking occurs where, in the thermal history of the material, the tensile stress exceeds the ultimate strength of solid material (Carter et al., 2014; Harrison et al., 2015). Figure I.0.4 shows delamination, which is a particular case of cracking where cracks originate and propagate between adjacent layers (Grasso & Colosimo, 2017). Delamination occurs when residual stresses exceed the binding ability between top and bottom layers (Zäh & Lutzmann, 2010).

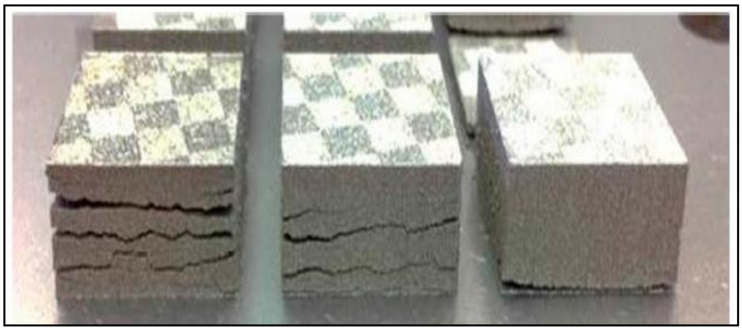

Figure I.0.4 Delamination and cracking (Grasso & Colosimo, 2017)

Geometric and surface defects: The PBF-produced parts may exhibit dimensional, geometric and surface inaccuracies and deviations. Figure I.0.5 below shows these defects (Grasso et al., 2017). Both part shrinkage and volume enlargement are common phenomena (Sharratt, 2015). In addition to that, different kinds of warping were also discussed. A combination of warping and shrinkage, called the curling phenomenon is also seen in some parts (Mousa, 2016). Curling is associated to an uneven shrinkage between top and bottom of the part. (Kleszczynski et al., 2012) investigated the formation of super elevated edges, i.e. elevated ridges of the solidified material at the edges. This does not just deteriorate the surface topology and dimensional accuracy but also interferes with the recoating system, increasing its wear and negatively affecting the powder bed uniformity (Yasa et al., 2009). Other distortions include critical features like thin walls, overhanging surfaces and acute corners (Grasso et al., 2017b). In these regions, the melt pool is largely surrounded by loose powders which has a lower thermal conductivity. The diminished heat flux gives rise to local over-heating that again hampers the geometry.

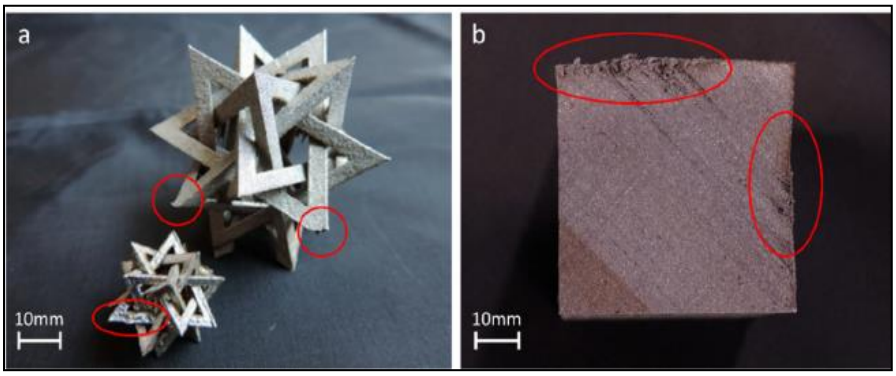

Figure I.0.5 Geometric defects (a) and Surface defects (b)(Grasso et al., 2017)

The PBF-produced parts are usually post-processed for surface and thermal treatments, as surface finishing is technologically relevant due to its effect on fatigue performances of the part. Because of this, out-of-control roughness and surface characteristics represents a major defect in the PBF process (Sames et al., 2016). In the PBF process, surface roughness has two contributions: (1) the 'stair-stepping' effect due to layer-wise production and (2) the actual roughness of the metal surface. The surface finishing depends upon the surface orientation with respect to the growth direction. Surface defects are also produced by balling effect (R. Li et al., 2012).

Chapter II
Experiment building: Infrared thermography

II.1 Introduction: Basics of thermography

Infrared (IR) thermography is one of the most commonly used non-invasive type temperature measurement methods in LPBF. An Infra-red camera, also known as thermal camera, is a type of infra-red thermography. All objects above absolute zero (0 Kelvin) emit infrared radiation, which the IR sensors use to measure the temperatures. In the Electromagnetic (EM) spectrum, the Infra-red regime is between 0.8 µm and 14µm. The IR camera sensor detects the infra-red radiation, converts it into electrical signals and displays the equivalent temperature. The pixels in a thermal camera correspond to separate sensors placed together in a Focal Plane Array (FPA), each collecting the EM radiation from the object being measured. The radiation emitted by the object can be characterized by two features: wavelength (λ) and intensity (Q). Objects at a particular temperature emit radiation over a range of wavelengths. Converting the intensity of the collected radiation to temperature is complicated by the emissivity of the observed object. In heat transfer, a 'blackbody' is a theoretical object that radiates the maximum possible energy for its given temperature. The intensity of radiation resulting from a blackbody at a certain temperature is given by Planck's law as follows:

$$B = \frac{2hc^2}{\lambda^5} * \frac{1}{e^{\left(\frac{hc}{\lambda kT}\right)} - 1} \quad (1)$$

where B is the spectral radiance (amount of energy emitted at different radiation frequencies), T is the absolute temperature, k is the Boltzmann constant, h is the Planck's constant, λ is the wavelength and c is the speed of light. The above expression shows for a blackbody, how radiated energy emitted at shorter wavelengths increases rapidly with temperature than energy emitted at longer wavelengths. Figure II.1 shows the intensity of emission from a solid at different temperatures. Note that, the higher the temperature, the peak λ (λ_{max}) is shifted towards left (lower wavelengths) and the larger the area under the curve.

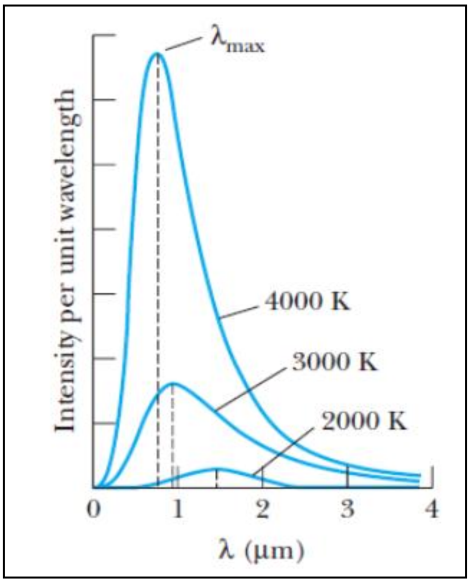

Figure II.1 Spectral distribution of blackbody at various temperatures (source: 'Modern Physics' by Raymond A Serway, Thomson Learning 2005)

For shorter wavelengths, Wien's displacement law accurately describes the spectrum of thermal radiation. Once we know the λ_{max}, it is possible to obtain the equivalent temperature using Wien's displacement law, as shown below:

$$T = \frac{b}{\lambda_{max}} \tag{2}$$

where b is the Wien's displacement constant (2.897 x 10^{-3}m K). Practically, no object radiates to its maximum possible energy. For example, if an object at a certain temperature radiates 80% of the maximum possible, the object is said to have an emissivity of 0.80. Therefore, when determining the object's temperature, the object's emissivity must also be considered along with the intensity of the captured radiation. An object's emissivity changes with temperature, surface finish, the state of the material itself (solid/liquid/gas) and the angle of observation. Especially when measuring over a 2D area with high temperature gradient, as in the case of our L-PBF, emissivity is highly non-uniform. Usually, a thermal camera is calibrated against a blackbody with an emissivity close to 1.0, to relate the camera signal to the blackbody temperature. Measuring the actual temperature of an object is rather difficult

and is mostly uncertain. A more straightforward approach is to capture the EM radiation and convert that to 'imagined temperature', assuming the object to be a blackbody. Identifying the true temperature requires the understanding of the object to be imaged and also the characteristics of the camera optics.
Based on the requirements, thermal cameras are widely classified into two types: Coaxial and off-axial sensing systems, and one can choose a commercially available thermal camera based on parameters to measure such as temperature measurement range, frame rate, wavelength (Near IR, mid-IR or far IR), the field of view and resolution. The coaxial system makes use of the optical path of the laser to study the heat affected area whereas in the case of off axial system, the sensor is mounted at an angle which gives an overall view of the powder bed (Grasso & Colosimo, 2017).

II.2 Process signatures

During the L-PBF process, which involves lot of heat exchange, the dynamic characteristics of the powder heating, melting and solidification processes are called the Process signatures (Mani et al., 2017). The observable process signatures are: (1) the melt pool, (2) the scan path, (3) the slice or layer, and (4) the powder bed.
1. The melt pool is a primary feature of interest as it involves beam-material interaction (Clijsters et al., 2014; Craeghs et al., 2010). The Melt pool-related characteristics that are of interest are: size (area or diameter), shape, temperature intensity and profile (1D, 2D). The melt pool properties determine the geometric accuracy of the track, porosity, and presence of un-melted particles, which also gives rise to residual stresses, cracking and delamination and, ultimately, the quality of the final product (Mercelis & Kruth, 2006; Zäh & Lutzmann, 2010). The melt pool represents the highest level of in-situ monitoring methods, which imposes different challenges from a measurement point of view: Firstly, the sensor should be able to measure the characteristics of a very small region (a few hundreds of microns of diameter) with sufficient spatial resolution. Secondly, a very high sampling rate (frame rate) is required as the scanning speed is a few hundred millimeter/second (Grasso & Colosimo, 2017).
2. Another important measurement is the laser track. The quantities of interest are track geometry, temperature profile and material ejected during the process. Tracking the information of the laser track is important to determine balling phenomena, lack of fusion, local overheating, and surface and geometric errors (Grasso et al., 2017; Kanko et al., 2016; Krauss et al., 2012). The monitoring of laser track is also challenging, similar to monitoring melt pool.

3. The 2-D temperature of the Layer is also an important feature in determining the irregularities caused by the lack of fusion or over-heating (Krauss et al., 2012; Moylan et al., 2014).
4. The 2-D temperature profile and the monitoring of the uniformity of the powder bed are additional features that can be used to characterize the spatial, and temporal evolution of the process and to detect rippling and grooves, respectively (Foster et al., 2015; Islam et al., 2013).
In exploring the above major properties, authors have used IR cameras to visualize the process overall temperatures, search for possible defects and implement feedback control to optimize the process (Craeghs et al., 2012; Delgado et al., 2012; Krauss et al., 2012). Most of the experimental papers have measured the relative temperatures (or imagined temperatures) and not the true temperature, mainly because of the emissivity issues. In order to validate the numerical models, as in our case, it is important to calibrate the sensor as we would need true temperatures. (Kolossov et al., 2004) compared experimental measurements with numerical models although there was no discussion about the calibration of sensors. Some authors (Fischer et al., 2004; Roberts et al., 2009) calibrated the camera using a pyrometer. (Williams et al., 2019) calibrated their FLIR A35 thermal camera using a calibration component made of the same material and parameters as the component to be investigated and used a k-type thermocouple on the surface. (Hooper, 2018) also used thermocouples for the calibration of sensing systems. Alldredge et al. (2018) discussed a new method of combining experimental and theoretical models without the need for measuring the true temperature of the surface. Although model validation cannot be done, they implemented a low-cost thermal imaging solution allowing for relative temperature measurements. These measurements are sufficient to detect unwanted process variability and to match these process variations with a faster than real-time qualitative reduced model that allows the process to be rapidly modelled during the build.

II.3 State of the art

An Infra-red camera with a very high frame rate can measure high-speed phenomena such as melt pool characteristics and spatter ejections very well. The camera frame rate specification depends on the image processing capabilities of a camera. The required field of view of the camera depends very much upon the amplitude of the layer area to be monitored. Smaller fields of view at constant resolution mean higher frame rates. A high-resolution camera will generate a high-quality image. The more pixels (detector elements) we have, the higher the resolution (therefore, more electromagnetic energy is gathered to display a detailed image). The temperature measurement range of the camera is also one of the key factors to be considered in achieving the objective. Table II.1 reports the types of IR cameras used and their corresponding properties.

Table II.1 Literature review on thermal cameras for L-PBF process

References	Camera	Wavelength	Field of view	Lens & Filter	Frame rate	Resolution	Monitored for
(Hagen et al., 2019)	FLIR SC-8200 IR camera	3-5µm	N/A	50 mm lens, ND2 filter (for high temp), ZnSe window	474 Hz	150 µm/pixel	Layer surface temperature
(Williams et al., 2019)	FLIR A35 IR camera/co-axial set-up	0.7-0.95µm	N/A	Germanium window	60 Hz	320 × 256 pixels	Layer surface temperature
(Dinwiddie et al., 2016)	FLIR SC-8200 IR camera	3-5µm	N/A	25 mm lens, IR transparent Sapphire window	N/A	N/A	slice Temperature/intensity profile
(Krauss et al., 2012)	Infratec Variocam	8-14 µm	160x120mm	50mm telephoto lens, Germanium and B270 super white glass	50Hz	250 µm/pixel	Melt pool Temperature/ intensity profile, slice Temperature/intensity profile

(Lane et al., 2016)	Extended sensitivity range InSb camera	1-5.3 µm	12.96x6.82mm	50mm short wavelength IR lens	1800	36 µm/pixel (horizontally) 53.3 µm/pixel (vertically)	Temperature/ intensity profile, ejected material
(Bayle & Doubenskaia, 2008; Doubenskaia et al., 2015)	FLIR Phoenix RDAS with InSb sensor	3-5 µm	6.4x13.6mm	25mm lens	2031-3556Hz	100 µm/pixel	Melt pool shape, Track geometry, Temperature/ intensity profile, ejected material
(Wegner & Witt, 2011)	InfraTec Jade III MWIR camera	3-5 µm	entire build area	50 mm telephoto	700hz	N/A	powder bed Homogeneity, temp intensity, profile, slice Temperature/intensity profile
(Gong et al., 2013)	LumaSense MSC640 NIR camera	0.78-1.08 µm	31x23mm	lens with 500mm working distance	60Hz	46.8µm/pixel (horizontally), 66.2 µm/ pixel (vertically)	Melt pool Temperature profile, Temperature/ intensity profile
(Alldredge et al., 2018)	Quantum Well Infrared Photodetector (QWIP)	8-12 µm	N/A	ZnSe glass	1.3kHz	128x128 pixels	Overall temperature

(Price et al., 2012)	LumaSense MSC640 NIR camera	0.78-1.08 µm	31x23mm & 5.3x4mm	Lens with (A) 500 mm work. dist. and (B) 350 mm work. dist.	N/A	47.6 µm/pixel (lens A) 8.3µm/pixel (lens B)	Melt pool Temperature Profile and size, Temperature/ intensity profile
(Ridwan & Keck, 2014)	FLIR A320 IR camera	N/A	N/A	ZnSe glass	N/A	830 µm/pixel	slice surface pattern
(Rodriguez et al., 2015)	FLIR SC645 IR	N/A	N/A	N/A	N/A	350µm/pixel	slice Temperature/intensity profile
(Mireles et al., 2015)	FLIR SC645 IR	N/A	N/A	N/A	N/A	260µm/pixel	slice surface pattern
(Santospirito et al., 2013)	N/A	N/A	N/A	N/A	N/A	N/A	Heat tracking of laser scanner
(Craeghs et al., 2012)	Co-axial setup	0.78-0.95 µm	N/A	N/A	N/A	N/A	Temperature maps due to thermal stresses
(Lott et al., 2011)	Co-axial set-up	N/A	1.79x1.79 mm, 3.58x3.58 mm	N/A	N/A	14µm/pixel	Melt-pool dynamics
(Ho et al., 2002)	Mikron® M67S infrared temperature sensor	N/A	N/A	50 mm focal length	5Hz	N/A	Average surface temperature measurements
(Gao et al., 2008)	Raytech MR1S	3–5 µm	N/A	N/A	25Hz	N/A	Average surface temperature measurements

(Hu & Kovacevic, 2003)	Co-axial set-up	0.7-1.06 µm	N/A	IR filter (>700nm) Nd:YAG laser blocker	300Hz	128X128 CCD	Melt pool temperature
(M'Saoubi & Chandrasekaran, 2004)	IR-CCD camera	0.4–1.1 µm	6.4	IR filter (800-1100nm)	N/A	752×582 pixels	investigate the role of tool micro-geometry, coating, cutting conditions and work material in orthogonal turning

Chapter III
Experimental building

III.1 Assembly components

Thermal camera: As a starting point, we procured a "Seek" thermal camera as we intend to test polymer powders which have a melting point of less than 300°C. The Seek thermal camera can measure temperatures between -40°C to 330°C, which is sufficient for polymer powder temperature measurements. It is mounted on a Raspberry-pi computer, as shown in Figure III.1. The communication architecture between the camera and the computer is shown in Figure III.2.

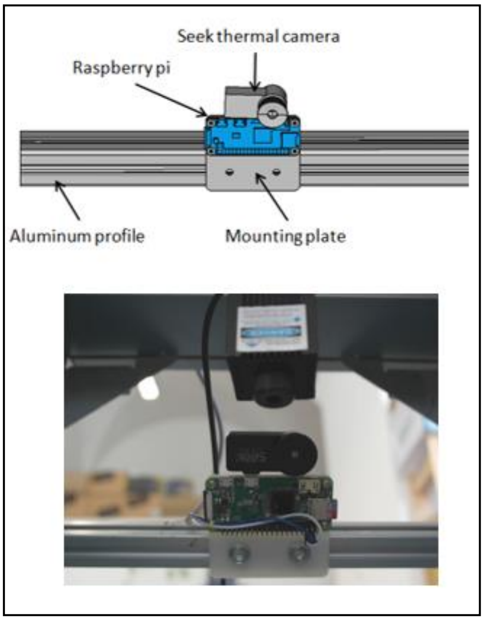

Figure III.1 CAD model of Seek thermal camera mounting

The Seek thermal camera has a resolution of 206 x 156 pixels with a field of view of 36 degrees. It measures in long-range IR between 7.5 to 14 microns and has a frame rate of less than 9Hz.
This camera is also quite compact and, thus, can be used inside the built chamber, especially when placed under the powder bed.
Laser: We have used LDM-405-1000 type 1-watt diode laser to conduct initial tests, which operates in the wavelength between 400 to 410 nm.
Temperature sensor: A high accuracy temperature sensor Bosch MCP9808 is used to measure the internal build chamber temperature, which will be cancelled out while measuring the actual powder bed temperature.

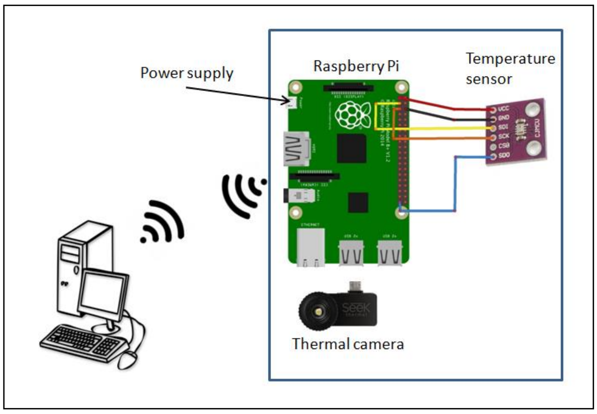

Figure III.2 Communication architecture for Thermal camera

Assembly set-up: The thermal camera was set-up inside the build chamber according to the procedure in the following. As a first step, we built an experimental set-up with a stationary laser source and fixed powder bed (1D condition). We have selected Polyamide 12 (PA12) as the powder material. The following Figure III.3 shows the Computer-Aided Design (CAD) assembly model made form 'FreeCAD' open-source software. Figure III.4 shows the actual experimental assembly.

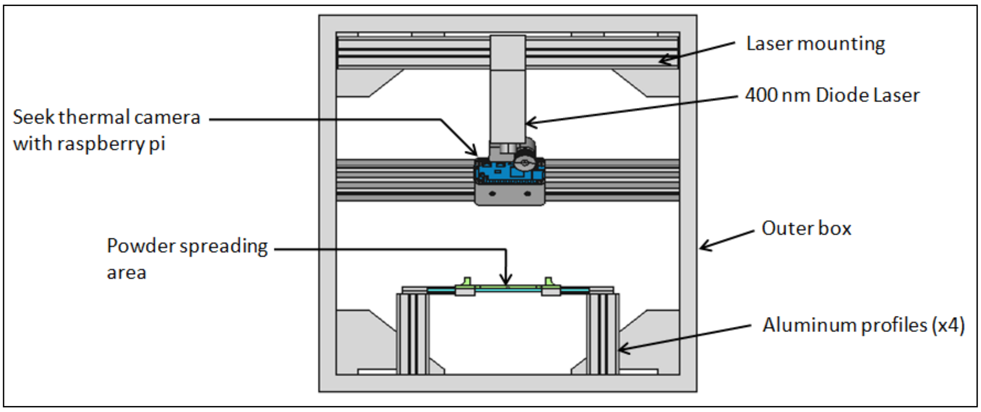

Figure III.3 CAD software model front view of experimental set-up

Figure III.4 Actual experimental build: Assembly (left) with door included (right)

The Laser is mounted on an aluminium profile which can be moved horizontally, although its position is fixed during the experiment. The Seek thermal camera is positioned at 45° angle and is mounted on 'raspberry pi', which in turn is mounted on aluminium profiles. The communication to control the camera is through Virtual Network Computing (VNC) viewer and Wi-Fi. The bottom assembly consists of a powder bed area with Quartz glass mounted using clamps (made of PolyLactic Acid using the Fused Deposition Modelling method of AM), which in turn is supported by four aluminium profiles. Door are used to cover the set-up during experimentation.

III.2 Materials

The polymer powder selected for the study is the carbon black treated Polyamide 12 (PA12 CB) (Sintratec AG) and carbon black treated Polyamide 6 (PA6 CB) (Ultrasint) which are two of the widely used materials. PA12 powder is an industrial grade polymer (Nylon) and has a density of 1100 Kg/m^3, melting temperature of 186°C and heat deflection temperature of 177°C. The carbon black is added in order to alter the laser absorptivity of the powder which has a loading of <1%. The optical properties of a powder bed are essential in understanding the laser material interaction in LPBF. The commercially available PA12 CB powder has a median particle diameter (d50) of 60µm and for PA6 CB, the median particle diameter (d50) is of 80µm. The particle size distribution of the powders are displayed below Figure III.5.

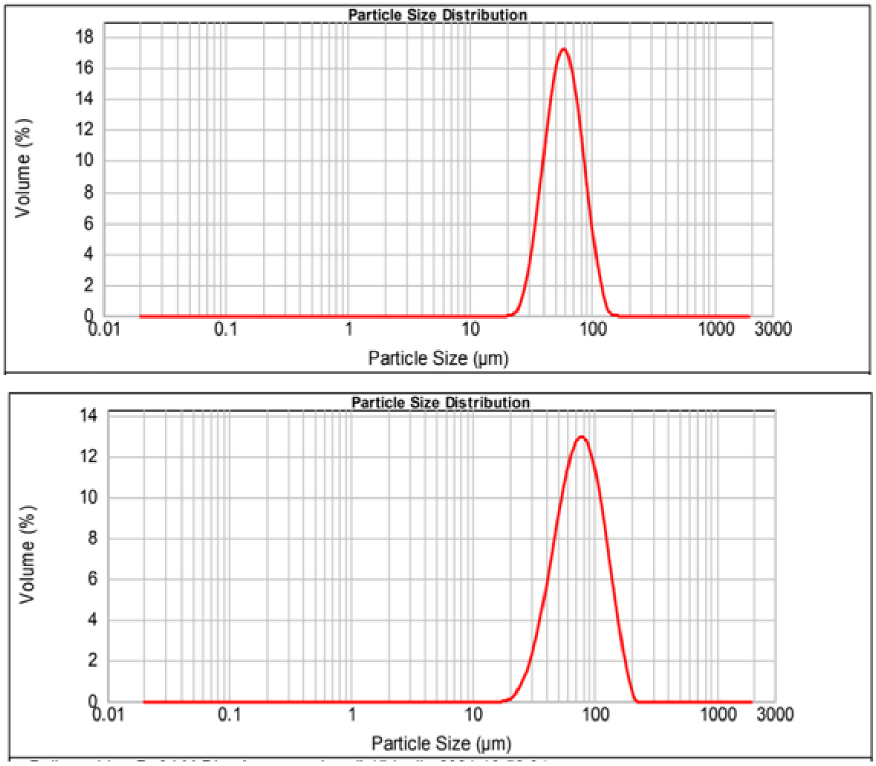

Figure III.5 Particle size distribution of PA12 CB (top) and PA6 CB (bottom)

Table III.1 Distribution of particle size by volume

Value	PA12 CB	PA6 CB
d10	0.00%	0.00%
d50	39.08%	33.12%
d90	52.13%	44.60%
d(3,2)	54.67µm	66.13µm
d(4,3)	61.00µm	80.20µm

Powder spreading: The powder bed spreading is done on top of Quartz glass with supporting parts as shown below. Polyamide 12 is spread on a 60mm x 60 mm area exposed to laser heating.

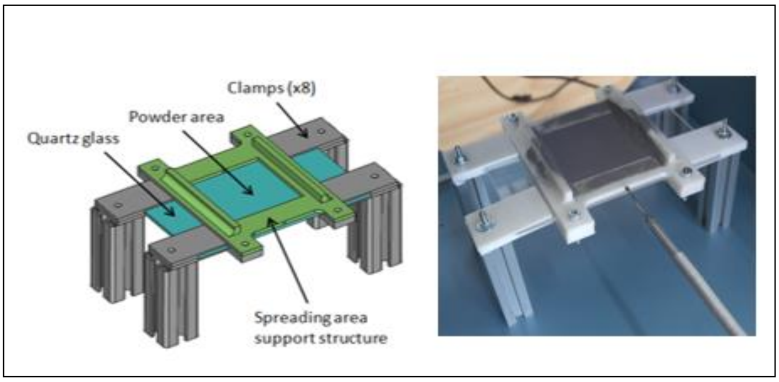

Figure III.6 CAD software model of Spreading assembly (left) and actual set-up with a thermocouple inserted (right)

The spreading area support structure is made of different thicknesses, which implies the direct powder layer thickness. We initially used 1mm and 3mm thickness for calibration of the thermal camera which also has provision for thermocouple insertion, but the thickness can be lowered down to 0.1mm. The main purpose of using quartz glass is also to conduct experiments with the thermal camera positioned below to visualize the laser heat penetration and the thermal profile into the powder bed and thereby estimate the vertical thermal penetration and the horizontal thermal propagation. The quartz glass is highly transparent to Infra-red and visible spectrum of EM radiation. We have used a 3mm thick quartz glass with a dimension of 150mmx100mm.

III.3 Initial results

Initial tests were carried out to test the proper working of the set-up. Polyamide 12 powder and Seek thermal camera were used for this purpose. Pixel-wise temperature matrix was extracted (206 x 156) from the sensor.
The following procedure was performed:

- Preparation of powder bed with PA12CB powder using the spreading tool
- Laser heating of powder bed at changing exposure times between 10 s is done
- Pixel-wise raw data measured by thermal camera is converted into sensible temperature information.

The pixel-wise raw data generated from the thermal camera and the corresponding temperature matrix is displayed below in Table III.2. Although the matrix is available for the entire field of view of the camera, the laser-illuminated spot and the heat affected zone is shown below. The Seek thermal camera uses an uncooled vanadium dioxide-based microbolometer, which is a type of infrared detector. The detector is sensitive to infrared energy, and once the element increases in temperature, the resistance changes, which is the directly measured variable that is processed to get temperature values. In this preliminary set of experiments with the PA12 tested the equation found to convert the RAW pixel data into useful temperature information is the following:

$$\text{Temperature}, \mathrm{T} = (0.015X) - 209.44 \quad (3)$$

where *X* is the RAW pixel value. Table III.3 shows the converted thermal image. This sensible temperature information in the heat affected zone is of importance as the temperatures are used to understand the heating and cooling at various times. The calibration of the thermal camera according to emissivity values are discussed in section III.6.

Table III.2 Laser illuminated spot: raw data matrix extracted from the thermal camera image (to be converted to temperature data)

17723	**17989**	**18275**	**18457**	**18595**	**18609**	**18615**	**18426**	**18123**	**17773**	**17567**
18212	18463	18793	19161	19369	19474	19082	19158	18806	18169	17929
18671	19152	19662	20103	20558	20591	20495	20173	19778	19087	18507
18993	19846	20602	21172	21828	21894	22134	21462	20931	19897	19263
19850	20721	21684	22602	23192	23479	23746	22947	22216	20988	19822
20346	21486	22633	23816	25485	25324	25951	24722	23464	22089	20618
20933	22131	23018	24290	25502	25992	25277	25541	25213	23128	21356
21235	22770	23952	25354	25012	25418	25406	25826	25355	23848	22026
21234	22722	24668	25559	25856	25499	25580	25835	25148	23972	22404
21170	22621	24299	25781	25240	25725	25636	25786	25753	23915	21934
21045	22266	23740	24981	25832	25899	25455	25304	25397	23378	21738
20484	21473	23088	24000	25063	25272	25263	24941	23907	22397	20857
20135	20971	21895	22848	23880	23948	24125	23586	22707	21371	20114
19240	19901	20583	21298	21989	22289	22382	22171	21612	20713	19788
18944	19493	19955	20464	20790	20930	20734	20545	19960	19156	18539
18599	18811	19162	19386	19695	19683	19694	19126	18871	18370	17937
18179	18196	18497	18646	18772	18724	18678	18391	18131	17816	17527

Table III.3 Laser illuminated spot temperature information in degree Celsius with a maximum temperature of 180.44 °C at the laser impact point

56.405	**60.395**	**64.685**	**67.415**	**69.485**	**69.695**	**69.785**	**66.95**	**62.405**	**57.155**	**54.065**
63.74	67.505	72.455	77.975	81.095	82.67	76.79	77.93	72.65	63.095	59.495
70.625	77.84	85.49	92.105	98.93	99.425	97.985	93.155	87.23	76.865	68.165
75.455	88.25	99.59	108.14	117.98	118.97	122.57	112.49	104.525	89.015	79.505
88.31	101.375	115.82	129.59	138.44	142.745	146.75	134.765	123.8	105.38	87.89
95.75	112.85	130.055	147.8	172.835	170.42	179.825	161.39	142.52	121.895	99.83
104.555	122.525	135.83	154.91	173.09	180.44	169.715	173.675	168.755	137.48	110.9
109.085	132.11	149.84	170.87	165.74	171.83	171.65	177.95	170.885	148.28	120.95
109.07	131.39	160.58	173.945	178.4	173.045	174.26	178.085	167.78	150.14	126.62
108.11	129.875	155.045	177.275	169.16	176.435	175.1	177.35	176.855	149.285	119.57
106.235	124.55	146.66	165.275	178.04	179.045	172.385	170.12	171.515	141.23	116.63
97.82	112.655	136.88	150.56	166.505	169.64	169.505	164.675	149.165	126.515	103.415
92.585	105.125	118.985	133.28	148.76	149.78	152.435	144.35	131.165	111.125	92.27
79.16	89.075	99.305	110.03	120.395	124.895	126.29	123.125	114.74	101.255	87.38
74.72	82.955	89.885	97.52	102.41	104.51	101.57	98.735	89.96	77.9	68.645
69.545	72.725	77.99	81.35	85.985	85.805	85.97	77.45	73.625	66.11	59.615

63.245	63.5	68.015	70.25	72.14	71.42	70.73	66.425	62.525	57.8	53.465

Figure III.7 (Left) Thermogram of powder bed with Laser illuminated spot (Right) specimen from melting PA12 CB

Figure III.7 shows the corresponding thermogram recorded by the thermal camera. As we can see from the above table, there is a huge thermal gradient between the laser-illuminated spot and nearby areas. The maximum temperature reached as per Seek thermal camera is 180.44°Celsius, which is nearly the melting temperature of PA12. This kind of information can be used to decide if the particles need to be sintered or melted. The shape of the specimen obtained is spherical, with sizes ranging from 1.5 to 1.8 mm for various exposure times.
The distance between each pixel is measured using the Instantaneous Field of View (IFOV). The IFOV is an angular projection of just one of the detector's pixels in the IR image and is measured in mRad. The area each pixel can see depends on the target distance for a given lens. In our case, the camera is at 100mm from the powder surface, and the following equation is used to measure the pixel-pixel distance:

$$IFOV = \left[\frac{FOV}{No.of\ pixels}\right] * \ [\frac{\pi}{180} X1000] \quad (4)$$

From the data sheet of Seek thermal camera, the Field of View is 36 degree and the number of pixels in the horizontal field of view is 206. The above equation gives IFOV as 3.1mrad. Therefore, the IFOV in mm is calculated for a 100mm distance as follows:

$$IFOV\ (mm) = \frac{3.1}{1000} * 100 = 0.31mm \quad (5)$$

Therefore, the distance between pixels is measured to be 0.31mm, and the**Error! Reference source not found.** is seen with the heating and cooling o f the laser heating zone. A high gradient can be seen at around 10mm diameter from the centre.

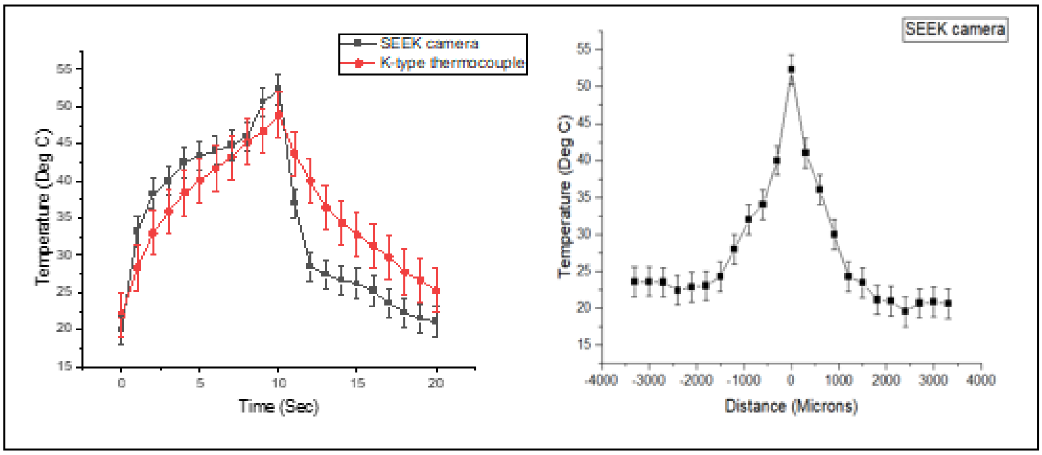

Figure III.8 PA12 CB data: Temperature at 1mm below the surface versus time: comparison between SEEK thermal camera and K-type thermocouple data (left) and pixel-wise temperature at 1mm below the surface at t=10s (right)

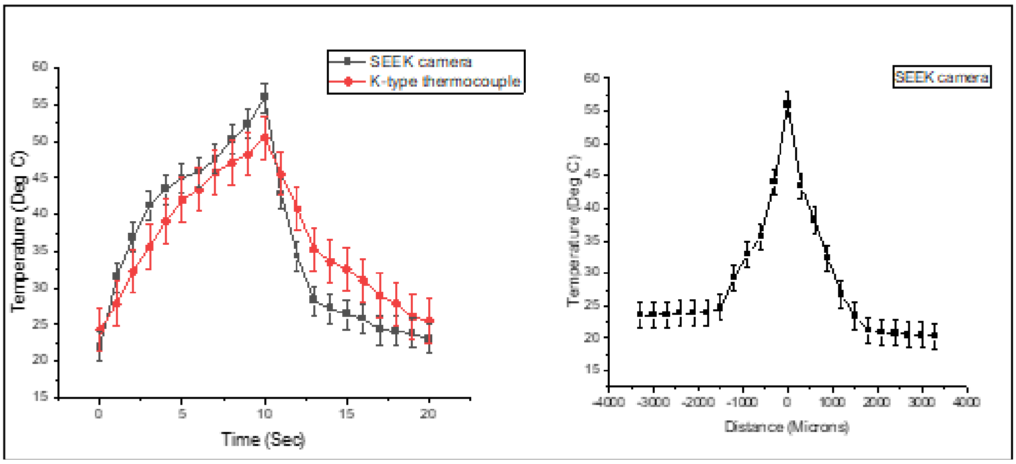

Figure III.9 PA6 CB data: Temperature at 1mm below the surface versus time: comparison between SEEK thermal camera and K-type thermocouple data (left) and pixel-wise temperature at 1mm below the surface at T=10s (right)

Figure III.8 shows the temperature recorded by the SEEK camera at 1mm below the surface after laser heating for 10s. A one-standard deviation error bar is calculated, and the error in the peak temperature zone is less compared to the heating and cooling areas. Also, the K-type thermocouple data measuring the temperature at 1mm below the powder surface is presented as a comparison. It can be found that the K-type thermocouple has a much larger error during the measurement due to the slender nature of the thermocouple, which tends to bend when inserted into the powder bed (as shown in Figure III.6). The cooling down phase captured by the thermocouple is also slower compared to the thermal camera due to the slower response of the same. From Figure III.8 and Figure III.9, it can be seen that the maximum temperature achieved after a 10s laser heating is slightly higher for the PA6 CB powder. This might be the reason that the PA6 CB has a higher absorption coefficient than the PA12 CB powder. Also, the temperature profile from the centre of laser impact is slightly wide spread for PA6 CB, meaning the PA6 CB might have a slightly higher thermal conductivity. The thermal conductivity data for both PA12 CB and PA6 CB are measured in section IV.4.1.

III.4 Experimental design maturity

In order to integrate the second thermal camera Optris Xi 400, its calibration to validate the same before using is essential. The powder surface emissivity varies with temperature, and an experimental set up to calibrate the cameras has been proposed. This section provides the calibration required for the Optris Xi 400 thermal camera. This high-efficiency thermal camera will be used as the primary thermal camera and also to monitor the top powder surface heating and cooling. The Optris Xi 400 has a very good optical resolution of 382x288 pixels and a spectral range of 8 - 14 microns. The camera works in the temperature range from 0-250°C or from 250-900°C. For our application with polymers, we use the camera in the former temperature range. It also has a frame rate of 27Hz or 80Hz and a field of view of 18° x 14°.

III.4.1 *Heated powder bed set-up*

A heated powder is used to calibrate the Optris thermal camera in order to take into account the variation of emissivity with respect to powder surface temperature. Two aluminium heaters are sandwiched between two aluminium plates, as shown in Figure III.10. The top aluminium plate is covered with a Kapton film in order to have uniform heating on the surface. The heating system is mounted on aluminium profiles as shown in Figure III.11. Care has been taken in order to keep the heating system isolated from aluminium profiles to avoid heat losses. Two rails are mounted in the system to facilitate powder spreading on the top of the heated plate. The heaters are controlled by PID controller in order to maintain a suitable temperature during the testing. The effect of the angle of view of the thermal camera with the powder surface emissivity has been neglected.

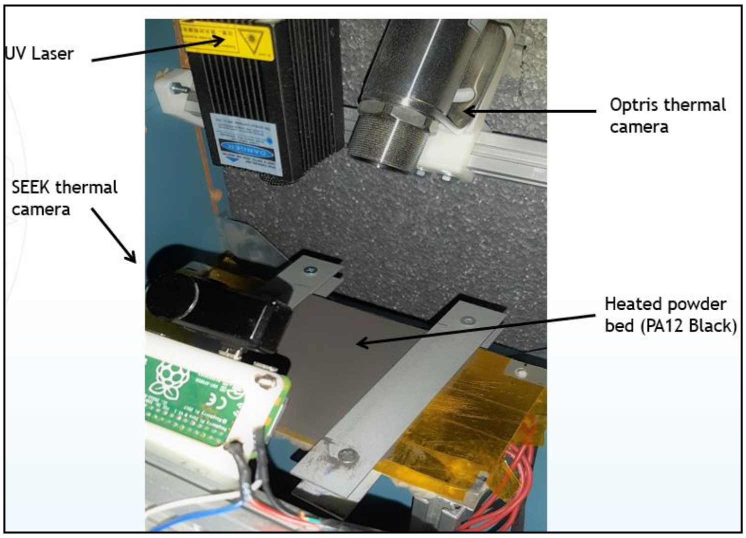

Figure III.10 Integrated thermal cameras: Optris Xi400 and SEEK, overlooking the PA12 CB powder bed

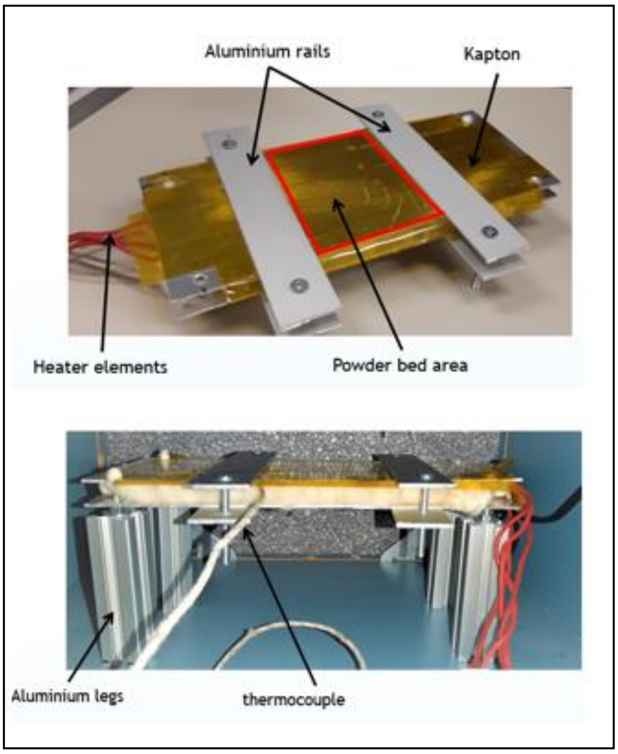

Figure III.11 Powder bed with heating system (top) and mounted on aluminium legs (bottom)

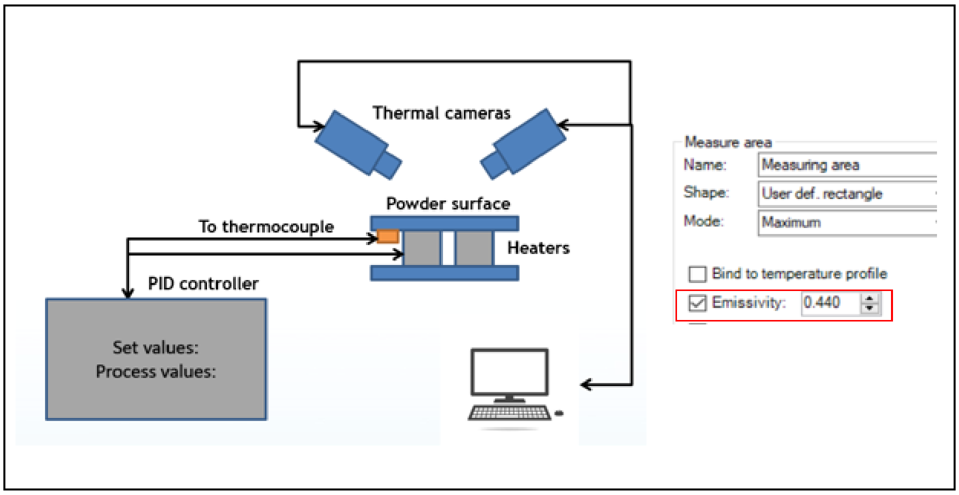

Figure III.12 Block diagram of the calibration set-up (left) and the provision to adjust the emissivity in the Optris thermal camera (right)

III.4.2 Calculation of steady-state heating of powder surface

Before starting the calibration of the cameras, it is important for the powder bed to reach the steady-state temperature. Therefore, the time taken to reach the steady-state for the powder bed for various temperatures is identified using a physical three-dimensional model of the heat transfer solved by means of COMSOL, whose details are reported in section III.4.1. Tests were conducted on PA12 black powder, and Figure III.13 shows the time taken to reach steady-state. The used heaters are good enough to reach steady-state in less than 250 s in most cases.

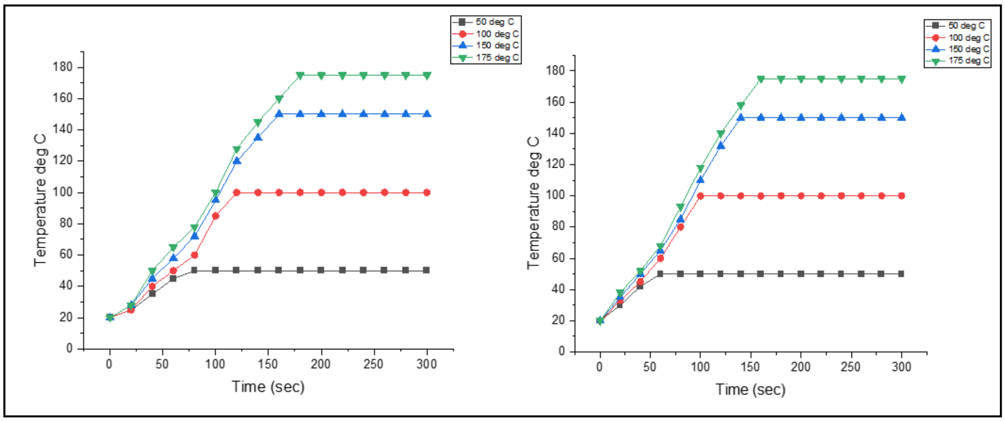

Figure III.13 Temperature change versus time in powder surface for PA12 CB after setting the heaters temperature: results obtained by heat transfer model predictions

III.5 Reassembling the experimental set-up

As a next step, the powder bed is prepared on top of a 1.5mm thick, anti-reflection coated Zinc selenide (ZnSe) window, which is transparent to the infrared radiation from 8 to 14 microns. The ZnSe has a very high transmissivity of 95% in this wavelength range, as shown in Figure III.15. The SEEK thermal camera is positioned below the powder bed in order to visualize the heat penetration in the powder bed. The block diagram of the reassembled experimental setup is shown below in Figure III.14.

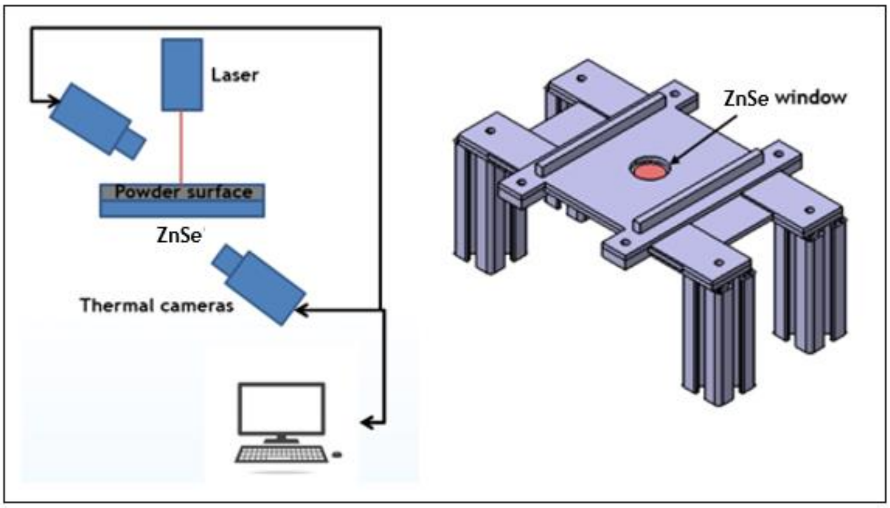

Figure III.14 Block diagram of the reassembled experimental set-up (left) and the CAD model with the ZnSe window installed (right)

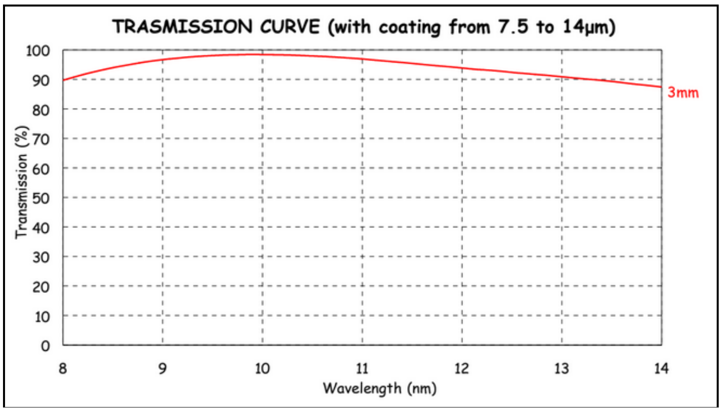

Figure III.15 Transmissivity of the ZnSe window provided by the manufacturer.

The above set-up, therefore, can be used to visualize the temperature distribution in XYZ directions of the powder bed. The pixel-to-pixel distance in the thermal image of the Optris camera position 100mm from the target is found directly from the datasheet to be 0.1mm

III.6 Measurement of the powder bed emissivity

Before to carry out experiments of heating on powder bed, measurements of the emissivity of the powder bed of PA12 CB and PA6 CB and its variation with temperature were done. The following procedure was performed thereby to calibrate the Optris thermal camera:

1. The heaters controlled by the PID controller heat the powder bed. The set values used are 50°C, 75°C, 100°C, 125°C, 150°C and 175°C.
2. Heating proceeds until the powder bed reaches the steady-state temperature.
3. The Optris thermal camera is used to measure the surface temperature. If the current reading is different from that of the set value, the emissivity is changed in the Optris software till the actual temperature is read. The procedure is repeated for various set temperature values.
4. The SEEK thermal camera is once again verified for calibration with the help of the calibrated Optris camera.

The results are displayed in the graph below of Figure III.16. It can be noticed that the emissivity is constant in PA12 and PA6 black powders as the temperature increases. As the temperature nears the melting point, the emissivity drastically increases. Although care has been taken in maintaining the temperature in the heating system, there has been frequent fluctuations of +/- 2°C due to heat losses.

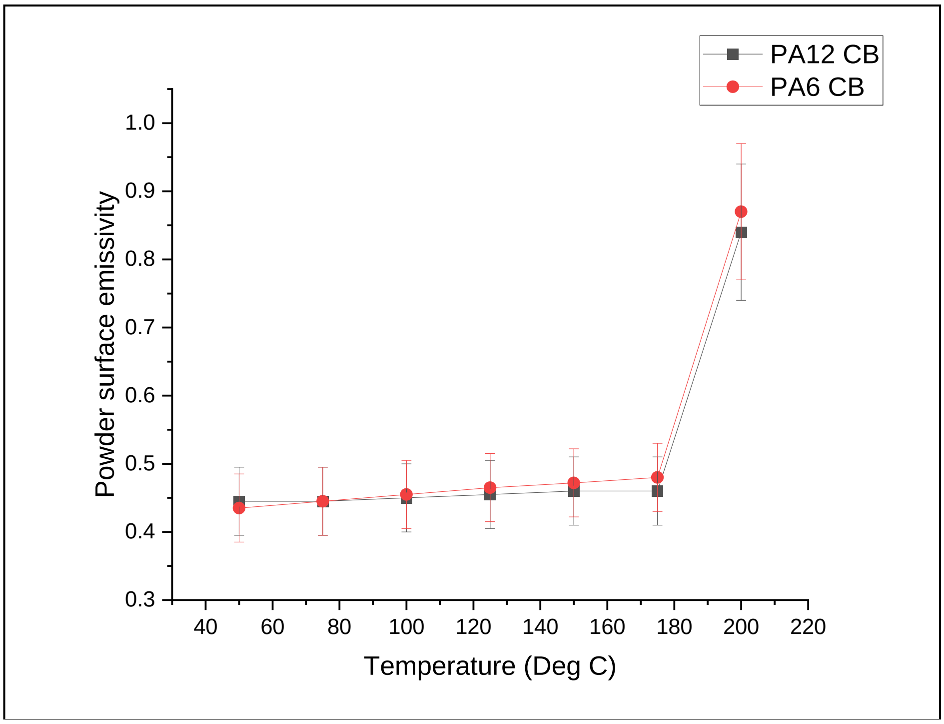

Figure III.16 Powder bed surface emissivity vs temperature for PA12 CB and PA6 CB. It can be seen that the emissivity is quite constant as the temperature increases and abruptly increases at the melting point

III.7 Transient heat transfer experiment with external energy provided by the laser

Before the experiments using the laser as way for heating, the Optris thermal camera is employed to measure the temperature history of the powder bed. The experiments were conducted by heating the bed with the laser and allowing it to cool down. The transient process is captured by the thermal camera. The emissivity value used from the calibration experiments was discussed in the previous section. Unfortunately, the emissivity is given as a constant value in the thermal camera, as there is no provision to input as a function of temperature. The following steps were performed while conducting the experiments:

1. Preparation of a uniform powder bed with PA12 CB and PA6 CB
2. Turning on the laser to heat the powder bed for 10 s and allowing it to cool down later.

3. Simultaneously, the thermal camera is used to capture the heating and cooling.
4. Processes 1-3 are repeated three times to verify the repeatability of the experiment.

At the end, the temperature versus time data are collected and illustrated in Figure III.17-18 for both powders. Figure on the left below reports the trend of the temperature for the three experiments conducted on PA12 CB powder and on the right the mean temperature of the tests. We see good repeatability of the tests, and this data is used for the model purposes.

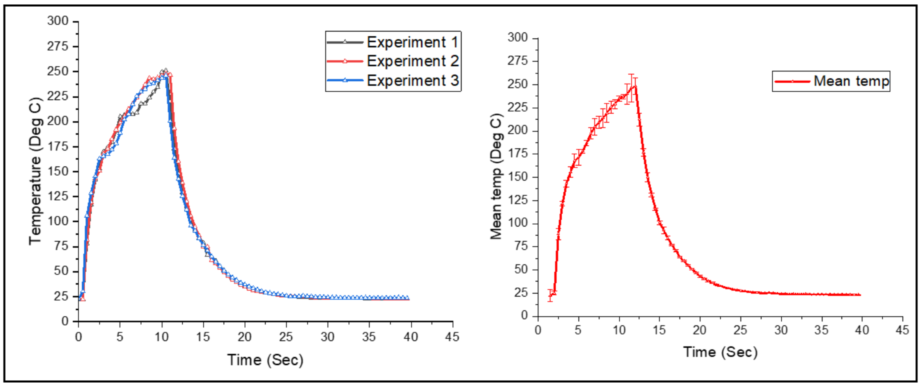

Figure III.17 Powder bed surface temperature transient behaviour: Temperature vs Time for 10s laser heating of PA12 CB.

Figure III.18 below describes the laser heating profile of PA6 CB. Compared to PA12 CB, PA6 CB exhibits a different heating/cooling transient for a 10 s heating. The PA6 CB absorbs more laser energy in its UV spectrum and converts it into heat very rapidly and maintains a steady state peak temperature of 275°C, which is higher than the PA12 CB. Once the laser is turned off at 10 s, the cooling happens rapidly as shown at 25.4°C/s, whereas the PA12 CB cools at 22.2°C/s. This may be due to a higher thermal conductivity of the PA6 CB than that of PA12 CB.

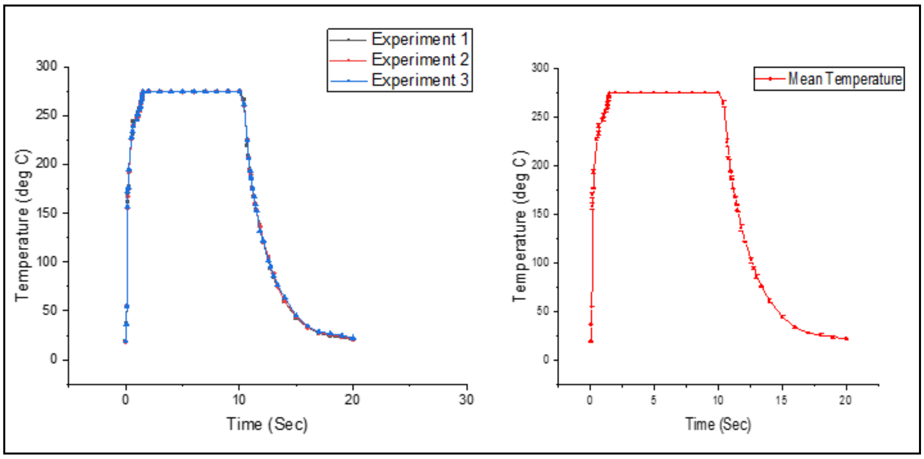

Figure III.18 Powder bed surface temperature transient behaviour: Temperature vs Time for 10s laser heating of PA6 CB.

III.8 Laser characterization

The characterization of the laser beam in terms of uniform distribution of power density in the powder bed is important in the experiments and while modelling the process. Therefore, the temperature distribution along the pixel-wise surface of the powder bed was measured with the Optris camera. Similar to the above procedure, three tests were conducted, and the distribution of temperature along the distance from the laser spot centre is shown in Figure III.19-20.

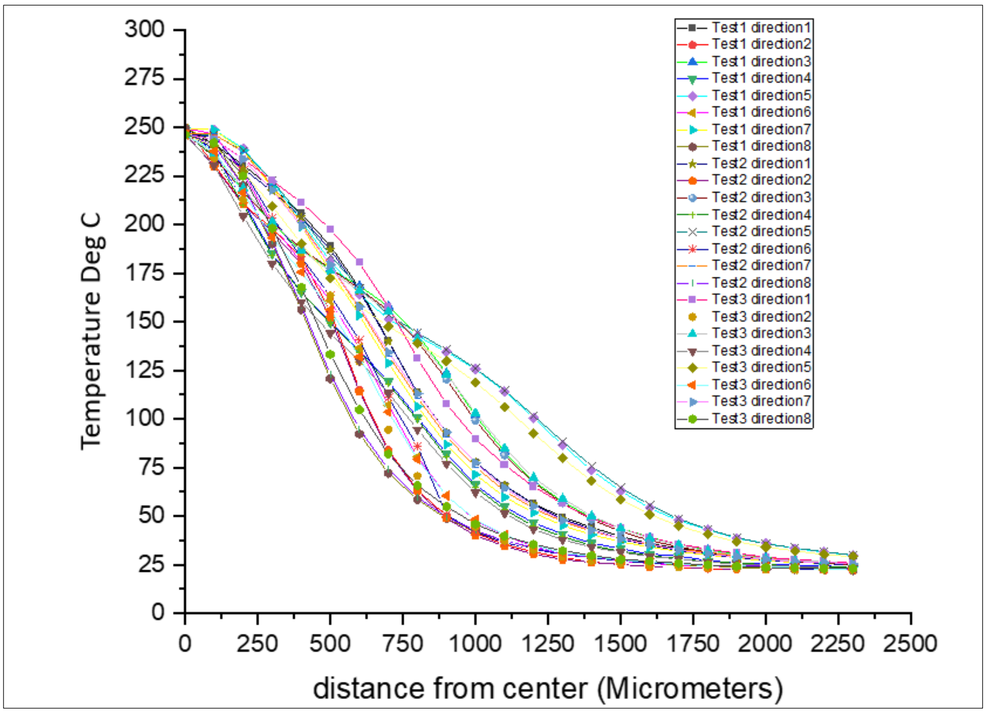

Figure III.19 Temperature spatial distribution on the powder bed surface at time t=10s

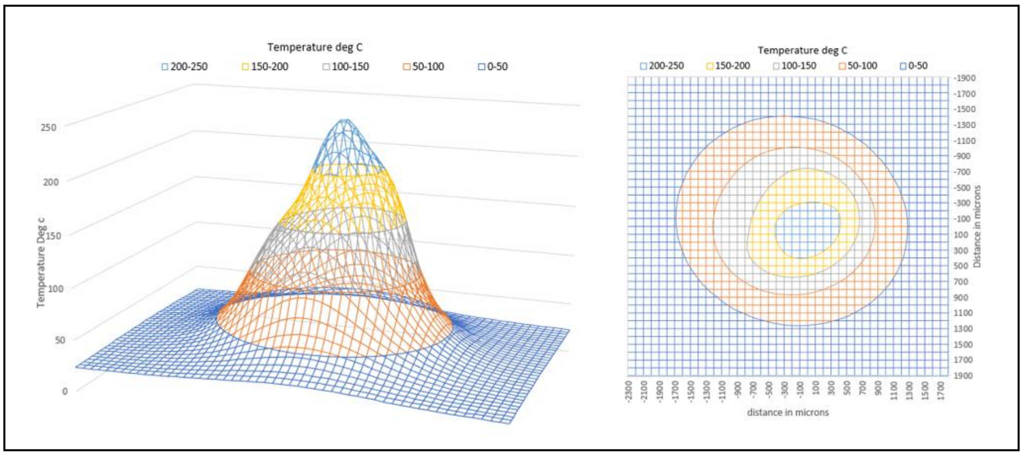

Figure III.20 Temperature spatial distribution on the PA12 CB powder bed surface at time t=10s (left) and the top view of the measured area (right). The skewed nature of the laser beam is visible here.

The laser beam intensity spatial distribution is usually represented as a Gaussian function with the intensity of the radiation diminishing to 1/e (or

37 %) of the original laser intensity value at a radial distance from the centre of the powder surface (Dowling et al., 2020). Instead, in our case, the temperature spatial distribution induced by the laser beam exhibits a skewed nature rather than a normal distribution which should be accounted for in the interpretation of the experimental results and in the modelling of the heat transfer phenomena.

III.9 Melt pool thermal conductivity

As the tests are conducted for a period of 10s, during which locally the temperature exceeds the melting point of the polymeric materials and the powder-to-melt pool phase change occurs, it is important to study the effect of the different value of the thermal conductivity of both the phases on the heat transfer. The experiment can be used in identifying the thermal conductivity of the melt pool in one direction as the process is assumed to reach steady-state after 10 s. As shown in Figure III.21, the temperature is nearly steady state after 8 s of heating in the case of PA12 CB and at 3 s in the case of PA6 CB (Figure III.22). This can be used to measure the temperature gradient from the centre of the laser impact towards the outer direction inside the melt pool. Until a distance of 500µm from the centre, the temperatures are well above the PA12 CB melting point of 186°C, and until 700µm from the centre, the temperatures are above the PA6 CB melting point of 193°C. Given the asymmetric nature of the heat distribution, the temperatures used in the calculation are in one direction only. Since the entire melt region reaches steady state, the temperatures are assumed to be constant in all directions.

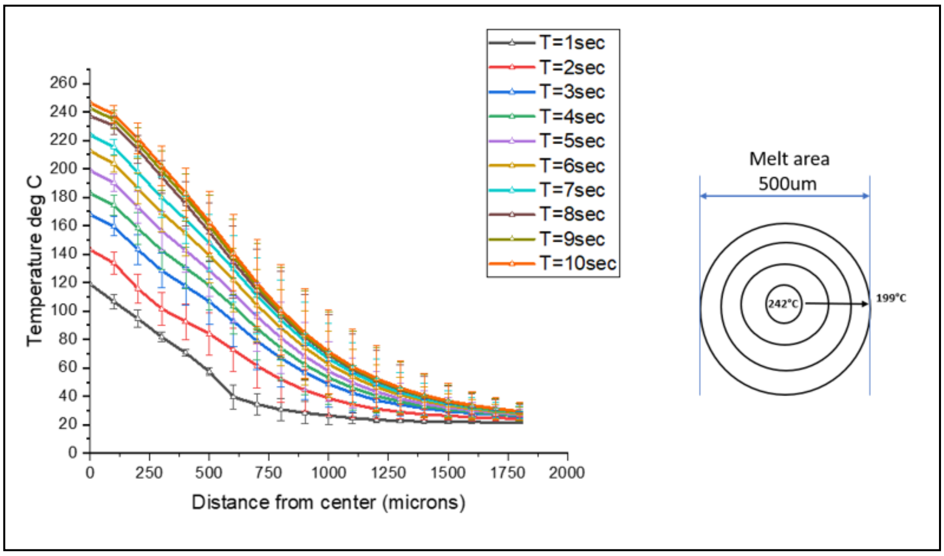

Figure III.21 PA12 CB: Temperature spatial distribution on the powder bed surface at various heating times (left) and the area used for the melt thermal conductivity measurement (right)

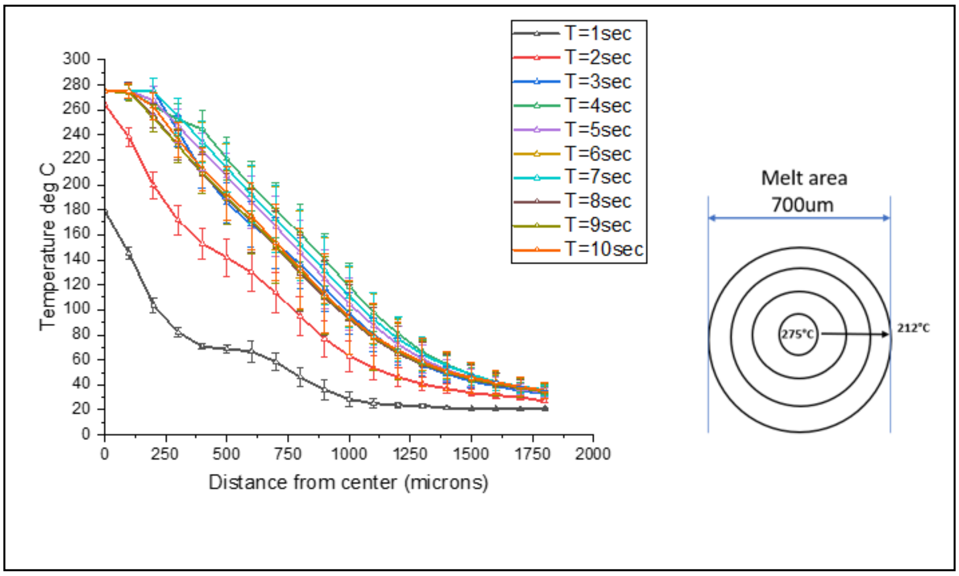

Figure III.22 PA6 CB: Temperature spatial distribution on the powder bed surface at various heating times (left) and the area used for the melt thermal conductivity measurement (right)

As we know the heat transfer in cylindrical co-ordinates is provided by the equation,

$$Q = \frac{2\pi LK(Ti - To)}{ln\frac{ro}{ri}} \tag{6}$$

where Q is the heat input, L is the length of the cylinder, K is the thermal conductivity, Ti and To are inner and outer temperatures respectively, ri and ro are the inner and outer radius of the cylinder. Therefore, in the case of a cylindrical melt pool, the liquid melt thermal conductivity along the cylindrical co-ordinates is calculated with the following formula:

$$Q = \frac{2\pi L(T1 - T4) * K_{liquid}}{\ln\left(\frac{r2}{r1}\right) + \ln\left(\frac{r3}{r2}\right) + \ln\left(\frac{r4}{r3}\right)} \tag{7}$$

where Q is the laser heat input, L is the thickness of the powder bed, $T1$ - $T4$ is the radial overall temperature gradient in the selected melt area, with a set distance from the centre. The value $T1$ is the temperature at the inner most point where the laser is impacted and the value $T4$ is the outermost temperature value of the cylinder where the temperature is safely above the melting temperature. The values $r1$ and $r4$ are the radius of the pixel size of the laser impact and the outermost radius of the melt cylinder, respectively. The distances between $r1$ - $r4$ is the concentric variation of pixel distances from the laser impact point taken from the thermal camera and K_{liquid} is the liquid melt thermal conductivity. Using the temperature data from the experiments, we get a value for the K_{liquid} of 0.403 W/mK for PA12 CB and of 0.52 W/mK for the case of PA6 CB.

Chapter IV
Thermal modelling

IV.1 Introduction

The thermal model is developed in order to accompany the experimental work. Based on the requirements, various thermal models can be employed to study the process. A particular type of model cannot cater to all different applications, such as temperature history, melt pool dynamics, residual stresses, powder bed generation, physical distortions and so on. The Table IV.1 below summarizes the type of model that can be used based on the applications:

Table IV.1 Existing Modelling approaches and their suitability on applications

		Model					
		FEM	FVM	LBM	SPH	DEM	Combined
Applications	Layer Temperature	Most suitable	Least suitable	Least suitable	Least suitable	Least suitable	Most suitable
	residual stress and distortions	Most suitable	Least suitable	Least suitable	Least suitable	Least suitable	Most suitable
	Phase transition	Most suitable	Most suitable	Most suitable	Most suitable	Most suitable	Most suitable
	Melt pool dimensions	Least suitable	Most suitable	Most suitable	Most suitable	Most suitable	Most suitable
	Balling/Non-uniformity	Least suitable	Most suitable	Most suitable	Most suitable	Most suitable	Most suitable
	Surface roughness	Least suitable	Most suitable	Most suitable	Most suitable	Most suitable	Most suitable
	Keyhole defects	Least suitable	Most suitable	Most suitable	Most suitable	Most suitable	Most suitable
	Porosity/densification	Least suitable	Most suitable	Most suitable	Most suitable	Most suitable	Most suitable
	Powder bed generation					Most suitable	Most suitable

(Legend: dark green = Most suitable; light green = Least suitable)

According to the table above, the FEM caters to the calculation of layer temperatures, residual stresses and phase changes in LPBF and can be combined with other models such as DEM to effectively. The FVM model is primarily used to study the melt pool dynamics. The LBM and SPH can also be used to study the melt pool and in fact, it treats the domain as particle nature. Other phenomenon such as surface roughness, porosity and keyhole defects can also be predicted with these models. The DEM is predominantly used in the powder bed preparation and also can be combined to calculate the other process parameters. The physics of LPBF considers the heat generated by the laser beam is transferred inside the powder bed through conduction, and some heat is lost in convection and radiation at free surface. The powder also undergoes phase changes such as melting and solidification (Figure IV.1). The basic theme of numerical methods is to make calculations at only a limited number of points and then interpolate the results for the entire domain, such as volume or surface. Even before getting the solution, we assume how the unknown variable is going to vary over a domain. After acquiring the results, there are ways to check numerical correlation accuracy and minimization of errors. The ultimate aim of these studies is to adjust the process parameters such as energy source input power, scan strategy and powder characterization for achieving products of desired qualities and minimizing manufacturing costs.

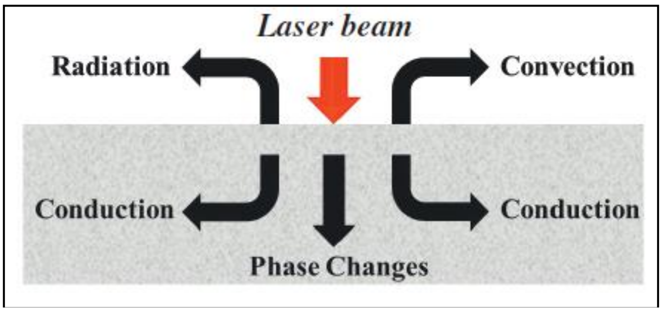

Figure IV.1 Modes of heat transfer in the SLS process (Sofia et al., 2015)

As described in Figure IV.2, the modelling is divided into micro, meso and macroscopic models based on the variations in spatial and temporal scales of the problems. The macroscopic thermo-mechanical models resolve the part-level residual stresses and deformations.

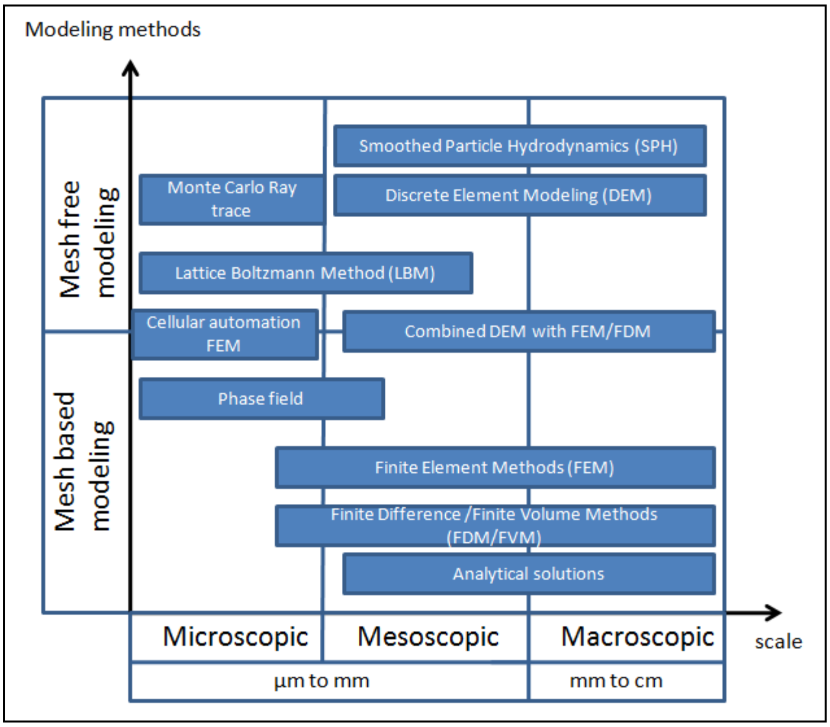

Figure IV.2 Different numerical simulations used in LPBF methods

IV.2 State of the art

The contents of this section were discussed more extensively in a paper (Soundararajan et al., 2021). A review of existing types of numerical simulations involving mesh-based continuum approach such as Finite Element methods (FEM), Finite Difference Method (FDM) and Finite Volume Method (FVM) (Meier et al., 2018) and discrete mesh-free approach such as Discrete Element methods (DEM), Lattice Boltzmann Method (LBM) and Smoothed Particle Hydrodynamics (SPH) is presented. The FEM was first initiated by Turner et al. (TURNER et al., 1956) and is a widely used simulation technique in PBF process (Krol et al., 2013) due to its simplicity and resource-efficient methodology, although it includes uncertainties, whereas the DEM was first discussed by PA Cundall et al. (Cundall & Strack, 1979) and is one of the least used yet promising technique for simulating PBF process, as this non-continuum approach better simulates the discrete nature of powder bed (Dayal & Gambaryan-Roisman, 2017). In the FEM model, a continuum domain is discretized into a finite number of elements, thereby forming a mesh, which reduces the problem to that of an equivalent finite number of unknowns (Madenci & Guven, 2006). The FEM has become a widely used technique for predicting porosity, residual stresses and distortion of parts produced by the PBF process (Schoinochoritis et al., 2017). Other numerical simulations, such as FDM, FVM and LBM methods, are primarily used to study the hydrodynamics of melt pool. Some commercial softwares used to solve are Ansys, Abaqus, Comsol, Fluent/CFX or custom-built codes. Monte Carlo (MC) method is also used to simulate heat absorption in the powder bed and ray tracing of the energy source. The DEM is a numerical approximation method for capturing the behaviour of particle interactions from a Newtonian mechanics perspective (Steuben et al., 2016) on single particles. It is one of the widely used numerical methods to simulate granular media (Luding, 2008; Mishra & Rajamani, 1992).

In LPBF simulations, the process can be simulated in a three-dimensional (3D) (Cheng & Chou, 2020; Karayagiz et al., 2019; Kolossov et al., 2004) or two-dimensional (2D) space (Matsumoto et al., 2002; Van Belle et al., 2012). Although most authors have used 3D to better simulate the realistic PBF process, some authors have used 2D to simulate a single layer as it involves lesser computational effects. Conduction is the main form of heat transfer, whereas radiation from the top surface has been neglected in some studies (J. Bai et al., 2015; Foroozmehr et al., 2016; Roberts et al., 2009) due to simpleness. Some authors have included radiation as well (P. K. Bai et al., 2006; Van Belle et al., 2012; D. Q. Zhang et al., 2010). The effect of phase change can be modelled by including the latent heat of material at the melting point (Hussein et al., 2013; Patil & Yadava, 2007; Shen & Chou, 2012). Phase changes also modify the material properties. In the FEM approach, powder particles can be modelled as a continuum property (Antony et al., 2014; Y. Li & Gu, 2014) or can be modelled explicitly as particles in the form of cubes stacked as powder bed (F. R. Liu et al., 2012). In DEM approach, each particle is treated individually and a part of the bed is represented by an array of N particles with desired size distribution (Gobal & Ravani, 2017; Steuben et al., 2016).
Following a continuum mechanics approach, the three-dimensional unsteady heat conduction in the powder bed is described by the following Fourier's law:

$$\frac{\delta}{\delta \mathrm{x}}\left(\frac{k\delta \mathrm{T}}{\delta \mathrm{x}}\right)+\frac{\delta}{\delta \mathrm{y}}\left(\frac{k\delta \mathrm{T}}{\delta \mathrm{y}}\right)+\frac{\delta}{\delta \mathrm{z}}\left(\frac{k\delta \mathrm{T}}{\delta \mathrm{z}}\right)+q=\rho C_p\ \frac{\delta \mathrm{T}}{\delta \mathrm{t}} \tag{7}$$

where k is the thermal conductivity (in an isotropic material is assumed, and it is uniform in all directions), T is the temperature, q is the rate of heat generation given to the system per unit volume, ρ is the density of the material (a further assumption is made on its constant value), C_p is the specific heat (also assumed to be constant), and t is the time. In order to consider the phase change, the modified heat capacity is used and given as

$$C_{pm} = C_p(T) + L_f f \quad (8)$$

Where $C_p(T)$ is the temperature dependent specific heat, L_f is the specific heat, f is the liquid fraction. The value of f is obtained as:

$$f = \begin{cases} 0, \; T < T_s \\ \frac{T-T_s}{T_L-T_s}, T_s < T < T_L \\ 1, \; T > T_L \end{cases} \quad (9)$$

Where T_s is solid temperature and T_L is liquid temperature.

The energy balance on top surface is subjected to two initial boundary conditions, firstly, heat generated is exchanged as conduction in the powder bed, convection and radiation to the ambient and can be written as follows:

$$-k\left(\frac{\delta \mathrm{T}}{\delta \mathrm{n}}\right) = h(\mathrm{T} - \mathrm{T_0}) + \sigma_b \varepsilon \left(\mathrm{T}^4 - \mathrm{T_0}^4\right) \quad (10)$$

Where n is the normal vector to the surface, h is the heat transfer coefficient of the gas medium, T_0 is the ambient temperature, σ is Stefan-Boltzmann constant, and ε is the surface emissivity. Secondly, the lateral surfaces are assumed adiabatic so that we can impose:

$$k\left(\frac{\delta \mathrm{T}}{\delta \mathrm{n}}\right) = 0 \quad (11)$$

Heat source model

To model the heat input, the intensity of the laser beam is represented as a Gaussian function given as:

$$q(x, y, z) = \frac{2AP}{\pi \mathrm{r}^2} \exp\left(-\frac{2(x^2 + y^2)}{\mathrm{r}^2}\right). \exp(-A(z)) \quad (11)$$

where A is the surface absorptivity of the powder bed, P is the power of the beam, r is the radius where intensity decreases from the intensity of the center by a factor of $1/e^2$. The temperature dissipation along the depth of the powder bed, z is given by the Beer-Lambert's law.

Masubuchi (Masubuchi & Agapakis, 1982) states that the all temperature-dependent material properties are a very important factor in the analysis of thermal stresses. Density is one of the most important thermo-physical properties as it influences thermal conductivity (Bugeda et al., 1999) and laser absorptivity of the powder bed (Shiomi et al., 1999). Density is a temperature-dependent property, and most of the time, the density of the final specimen is higher than the density of the powder bed (Kolossov et al., 2004). The relation between temperature and density is considered to be linear per Yin (Yin et al., 2012). Some authors have calculated the powder bed densities as follows (Antony et al., 2014; Patil & Yadava, 2007) :

$$\rho_{bed} = \frac{\pi \rho_{solid}}{6} \quad (13)$$

where ρ_{bed} is the bulk density of the powder bed and ρ_{solid} is the density of the solid.

Thermal conductivity is also a temperature-dependent property and is defined as the rate at which heat is conducted through the body and is usually measured as Watt per meter Kelvin. Thermal conductivity of powder is significantly different and lower than that of solid as the contact area between particles in the powder bed is smaller. Usually, in powder beds, an effective thermal conductivity is employed, which is dependent on various factors such as the size and the shape of particles, the solid volume fraction and the thermal conductivity of the interstitial gas (Shapiro et al., 2004). The powder bed's effective thermal conductivity is then calculated according to the porosity and thermal conductivity of gas in pores. The following equation describes the effective thermal conductivity of packed powder bed (Bugeda et al., 1999):

$$k_{eff} = \frac{\rho_r k_s(T)}{1 + \Phi k_s(T)/k_g} \quad (14)$$

where ρ_r is the relative density of the powder bed, relative to the equivalent solid density, k_s is the solid thermal conductivity as a function of temperature T, k_g is the gas thermal conductivity, and Φ is an empirical coefficient which is equal to $0.02X10^{2(0.7-\rho_r)}$.

Specific heat capacity is yet another temperature-dependent property and is defined as the amount of heat required to increase the temperature of one kilogram of material by one Kelvin. The specific heat capacity has a nonlinear relationship with temperature and phase change (Chen & Zhang, 2007). For the sake of simplicity, many authors have used linear interpolation or extrapolation (Kolossov et al., 2004; Song et al., 2012; D. Q. Zhang et al., 2010).

Latent heat is defined as the heat energy absorbed or released during a phase change. The temperature of the material is unchanged during the process. Thermal conductivity and specific heat change significantly during the melting of powders and while solidifying back to form tracks (Boivineau et al., 2006).

Table IV.2 State of the art: various models and their uses

Model type	Description	Inputs	Outputs	Limitations	references
Finite Element Methods	1. Assumes continuum powder bed, solves heat conduction equation sometimes considering radiation and convection 2. Melt pool hydrodynamics and associated effects are often neglected 3. Frequently used software: COMSOL, ABAQUS, ANSYS	Temperature dependent material properties Laser power, Beam size, Scan speed, Powder bed model, preheat temperature, optical properties of bed Solidus and liquidus temperature	Layer Temperature, residual stresses and distortions, Melt pool and heat affected zone dimensions	Not an accurate depiction of the PBF process, as FEM fails to replicate the particle nature of the system. Accurate analysis of melt pool formation is not possible and power spreading cannot be simulated	(Boillat et al., 2004; Contuzzi et al., 2011; Kolossov et al., 2004; B. Liu et al., 2011)

Computational Fluid Dynamics	1. Mass, Momentum and energy equations are numerically solved using FDM/FVM coupled with Volume of Fluids methods 2. Considers capillary, wetting, Marangoni effects, recoil pressure and vaporization 3. Frequently used software: FLUENT, OpenFoam and Flow3D	Temperature dependent material properties including latent heat of fusion and vaporization, Laser input, Powder bed model, preheat temperature, optical properties of bed Solidus and liquidus temperature, Surface tension coefficients and Gravity input	Layer Temperature, Melt pool dimensions, surface roughness, keyhole defects, porosity, balling and non-uniformity	Difficulty in implementation, longer computational times compared to FEM, poor representation of particle nature of the system, prone to numerical interpolation errors	(Khairallah & Anderson, 2014; Mokrane et al., 2018; Panwisawas et al., 2017; Wu et al., 2018)
Lattice Boltzmann Method	1. considers individual particles Solving discretized Boltzmann equation on a lattice,	Heat input, powder bed model, Temperature dependent material properties, viscosity	Layer Temperature, Melt pool dimensions, surface roughness, keyhole defects,	Choice of ideal lattice mesh is the basis to avoid numerical instabilities and in case of free-surface	(Ammer et al., 2014; Markl & Körner, 2018)

	2. Considers capillary, wetting, Marangoni effects, recoil pressure and vaporization		porosity, balling and non-uniformity	flows upgradation from 2D to 3D is not easy to implement	
Smooth Particle Hydrodynamics	1. Lagrangian mesh-free model in which governing equations are discretized by a moving set of particles 2. Highly adaptive in nature and suited in treating large deformation, moving interfaces and fluid-structure interactions and can provide the time dependent of the field variables.	Heat input, powder bed model, Temperature dependent material properties, viscosity, surface tension co-efficient	Layer Temperature, Melt pool dimensions, surface tension, thermo-capillary forces and phase changes	Prone to tensile instabilities, computationally expensive than FVM	(Fürstenau et al., 2020; Weirather et al., 2019)

Discrete Element modeling	1. Powder deposition and heat transfer studies possible 2. Well suited for realistic sintering/melting simulation of random packing of particles based on Newtonian interactions of a system of particles which includes contact models, friction and heat transfer, ability to establish/break inter-particle forces and influence of external forces 3. Some of the software used are LIGGGHTS, LAMMPS, EDEM	System of particles with geometry, heat input, temperature dependent material properties	powder bed preparation, Layer temperature, phase change/solidification	Computationally expensive, Lacks physical representation of Melt flow and convection is often nored	(Dayal & Gambaryan-Roisman, 2017; Steuben et al., 2016; Xin et al., 2017)

IV.3 Pre-processing:

In FEM, the pre-processing step is a critical step in formulating the problem statement. It involves describing the domain dimensions, meshing into finer elements of the domain, it's boundary condition such as ambient temperature, heat input model, material properties such as thermal conductivity, specific heat capacity and density which are temperature dependent as well, means of heat transfer such as conduction, convection and radiation and if phase changes are involved or not.

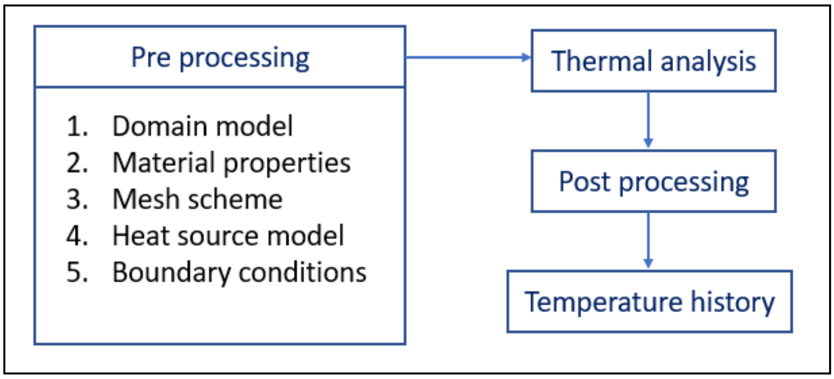

Figure IV.3 Flow chart of thermal analysis using FEM

IV.4 Finite Element based numerical model

A COMSOL-based FEM simulation is carried out to simulate the laser heating experimental set-up. The three dimensional heat conduction equation is written as :

$$\frac{\delta}{\delta x}\left(\frac{k\delta T}{\delta x}\right)+\frac{\delta}{\delta y}\left(\frac{k\delta T}{\delta y}\right)+\frac{\delta}{\delta z}\left(\frac{k\delta T}{\delta z}\right)+q=\rho Cp\ \frac{\delta T}{\delta t} \qquad (15)$$

Where k is the thermal conductivity (in an isotropic material is assumed and it is uniform in all directions and depends upon temperature), T is the temperature, q is the rate of heat generation due to laser, ρ is the temperature dependent density of the material, Cp is the specific heat (varying with temperature), and t is the time.

The initial condition is the standard room temperature and is given as,

$$T(x,y,z,t)_{t=0}=293.15\ K \qquad (16)$$

The initial boundary condition corresponds to the heat transfer between the top surface and the environment,

$$-k\left(\frac{\delta \mathrm{T}}{\delta \mathrm{n}}\right) = h(\mathrm{T} - \mathrm{T_0}) + \sigma_b \varepsilon(\mathrm{T})\left(\mathrm{T}^4 - \mathrm{T_0}^4\right) \quad (17)$$

where n is the normal vector to the surface, h is the convective heat transfer coefficient, T_0 is the ambient temperature, σ is Stefan-Boltzmann constant, and ε (T) is the temperature dependent surface emissivity. The heat transfer along the lateral sides of the powder bed are considered adiabatic,

$$k\left(\frac{\delta \mathrm{T}}{\delta \mathrm{n}}\right) = 0 \quad (18)$$

Where k is the thermal conductivity, T is the temperature and n is the normal vector. The laser input equation is provided as,

$$q(x, y, z) = \frac{2AP}{\pi \mathrm{r}^2} \exp\left(-\frac{2(x^2 + y^2)}{\mathrm{r}^2}\right).\exp(-A(z)) * B(t) \quad (19)$$

where A is the surface absorptivity of the powder bed, P is the power of the beam, and r is the radius where intensity decreases from the intensity of the centre by a factor of 1/e. $B(t)$ is the rectangular function corresponding to the time the laser is turned on (10s).

A precise estimate of the material properties helps in modelling the process more accurately. In order to identify the sensitivity of the material properties, such as thermal conductivity and laser absorptivity, the follow test matrix shown in Table IV.3 is used to conduct the simulations for PA12 CB since these values are not known. A variation of +/- 10% is considered from the mean value while the other parameters such as density, specific heat, laser power and laser diameter, are kept constant, and nine different combinations are tried. The thermal conductivity values K shown here were calculated as per section IV.4.1.

Table IV.3 Simulation test matrix for PA12 CB: 'k' represents thermal conductivity from section IV.4.1 and 'A' represents laser absorptivity

$k_i A_j$	k(W/mK)	A(1/m)
$k_1 A_1$	k_1	0.7
$k_1 A_2$	k_1	0.8
$k_1 A_3$	k_1	0.9
$k_2 A_1$	k_1+10%	0.7
$k_2 A_2$	k_1+10%	0.8
$k_2 A_3$	k_1+10%	0.9
$k_3 A_1$	k_1-10%	0.7
$k_3 A_2$	k_1-10%	0.8
$k_3 A_3$	k_1-10%	0.9

Table IV.4 Process and material properties of the PA12 CB powder bed that are temperature dependent or kept constant

Parameters	**Value**
Average particle size distribution	60µm
Density (temperature dependent, room temp value here) (Yuan et al., 2013) Solid, $rho(T) = -0.0005(T - 273) + 1.078$ *& liquid melt,* $rho(T) = -0.0006(T - 273) + 1.022$	1069 (Kg/m^3)
Specific heat (temperature dependent, room temp value here) $Solid, Cp(T) = 0.0163(T - 273) + 1.58$ & liquid melt, $Cp(T) = 0.0039(T - 273) + 3.214$ (Yuan et al., 2013).	1857 J/(Kg K)
Melting temperature	459 K
Latent heat of fusion (Yuan et al., 2013)	125000 (J/Kg)
Ambient temperature	20°C
Convective heat transfer (J. Bai et al., 2015)	25 W/m^{2}K
Emissivity (temperature dependent)	From experiments
Laser spot diameter	100µm
Laser power	1 W

Table IV.5 Process and material properties of the PA6 CB powder bed that are temperature dependent or kept constant

Parameters	**Value**
Average particle size distribution	80µm
Density (temperature dependent, room temp value here) (Yuan et al., 2013)	1370 Kg/m^3
Specific heat (temperature dependent, room temp value here) (Beyaz et al., 2022)	1750 J/(Kg K)
Melting temperature	193°C
Latent heat of fusion (T. Zhang & Kang, 2021)	190000 J/Kg
Ambient temperature	20°C
Convective heat transfer (J. Bai et al., 2015)	25 W/m^{2}K

Emissivity (temperature dependent)	From experiments
Laser spot diameter	100 µm
Laser power	1 W

IV.4.1 Powder bed thermal conductivity

The thermal conductivities of the powder bed are crucial in estimating the heat transfer profiles in the model. It is also complicated as the presence of interstitial gases which reduces the thermal conductivity by many folds. In the case of PA12 CB and PA6 CB, the presence of carbon black coating significantly alters the thermal conductivities. Also the radiative and convective heat transfer between the particles plays a vital role. Therefore, an effective thermal conductivity of the powder bed considering all the above is useful in better estimating the heat transfer. Based on (Trevisan et al., 2021), a two-particle-based thermal resistance model is used to estimate the thermal conductivity of PA12 CB. The carbon black is physically mixed with the PA12 powder, and the particles are ten times bigger than the carbon black (Espera et al., 2019). Our PA12 CB particles are 60µm. Therefore, the carbon black particles are assumed to be of 6µm. The carbon black is added by less than 4% by weight of the PA12, and the SEM images are shown below.

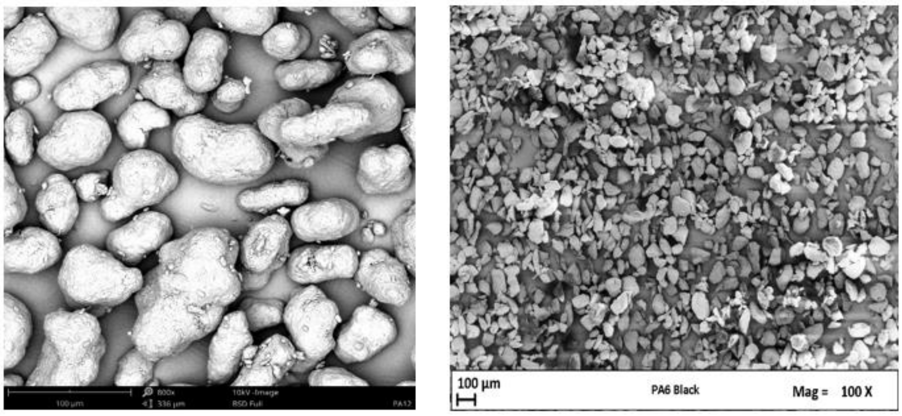

Figure IV.4 SEM images of PA12 CB (left) and PA6 CB (right)

The carbon black increases the thermal and electrical conductivities but decreases the mechanical properties of the final specimen if the carbon black added is more than 5% by weight due to inadequate physical contact between the main particles. The maximum number of carbon black particles on the surface of a PA12 spherical powder can be calculated as:

$$CB = \frac{4\pi(D^2/4)}{\pi(d^2/4)} \tag{15}$$

where D is the diameter of the main particle and d is the diameter of the carbon black particle. It can be theoretically estimated that a maximum of 400 carbon black particles are adhering to the PA12. Assuming a uniform thickness of 6 µm of coating, the PA12 thermal conductivity can be estimated as follows.

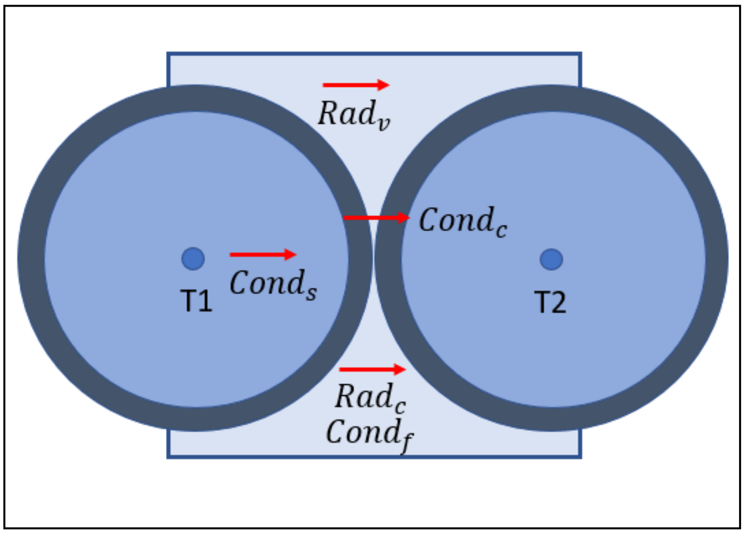

Figure IV.5 Two-particle effective thermal conductivity model with coating

The heat is conducted from the solid particle to the coating and then to the coating of the nearby particle, and then to the next particle, which resembles the resistance in series. There is a stagnant fluid layer in between the particles, and the other modes of heat transfer include radiation from the coating and radiation in the fluid region from void to void which form a parallel resistance network.

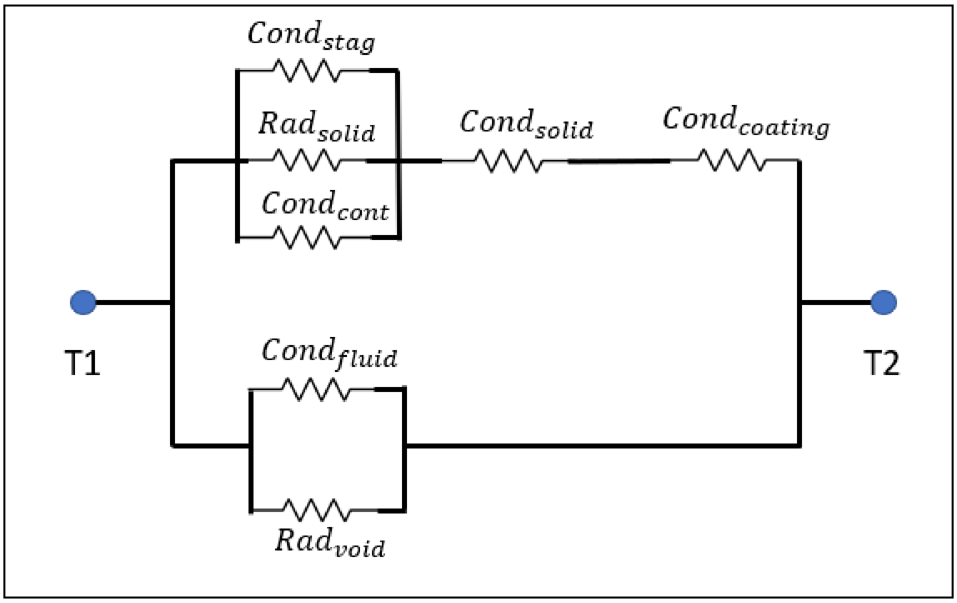

Figure IV.6 Thermal resistance model including various heat transfer modes between the two particles

The effective thermal conductivity is given as

$$k_{eff} = \mu\left[k_f + h_{rv}\Delta L\right] + \frac{[1-\mu]\Delta L}{\frac{1}{\frac{K_f}{l_v}+h_p+h_{rs}}+\frac{l_s}{k_s}+\frac{l_c}{k_c}} \quad (20)$$

where, μ is the void fraction of the powder bed, k_f,k_s and k_c are thermal conductivities of interstitial fluid, solid and coating, h_{rv} and h_{rs} are radiative heat transfer coefficient between voids and solids, ΔL is the distance between the centers of the particles, h_p is the heat transfer coefficient between the contact particles, l_v is the thickness of the fluid film in between the particles, l_s is the thickness of the solid PA12 that would provide resistance and l_c is the thickness of the coating. The interstitial gas in between is air and the heat coefficient varies with temperature. The values of h_{rv} and h_{rs} are defined as follows:

$$h_{rs} = 4\sigma T^3 \frac{\varepsilon}{2-\varepsilon} \quad (21)$$

$$h_{rv} = 4\,\sigma T^3 + \frac{\mu}{2(1-\mu)}\frac{(1-\varepsilon)}{\varepsilon} \quad (22)$$

Where σ is Stefan Boltzmann's constant and is equal to $5.67e-8\ W/m^2K^4$ and ε is the emissivity of the carbon black coating. The effective thermal conductivity is estimated to be 0.18 W/mK, which is higher than the normal PA12 powder estimated in (J. Bai et al., 2015). This value is at room temperature and a temperature-dependent thermal conductivity is important in the simulation. Therefore, the slope of the temperature-dependent curve of thermal conductivity is used from existing literature, and the estimated values are plotted in Figure IV.7.

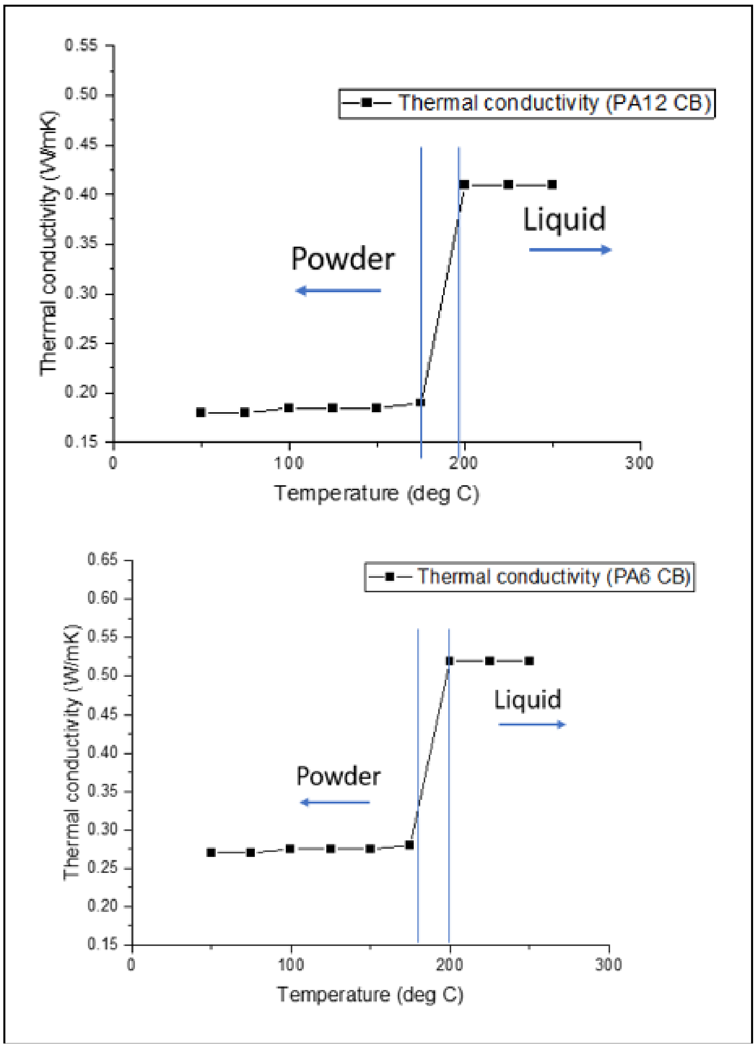

Figure IV.7 Thermal conductivity dependency on temperature used in the model for PA12 CB (top) and PA6 CB (bottom).

The effective thermal conductivity of the PA6 CB at ambient conditions is taken from (Beyaz et al., 2022) and then extrapolated are similar to other Polyamide powders in literature. The melt thermal conductivity was estimated in section 3.6.3. The thermal conductivities shown here are used as a base to perform a sensitivity analysis, as shown in the test matrix.

IV.5 Simulation domain

The quality of the domain meshing also influences the final results. Poor mesh quality may be the reason for erratic results and unstable solutions (Parthasarathy & Kodiyalam, 1991). Generally, the finer the mesh better are the results but at higher cost of computational time. Meshing can be ether uniform or non-uniform. Adaptive meshing is a type of non-uniform mesh scheme and one of the most used techniques used in FEM-based approaches. It is characterized by a mesh density that varies across different regions (Luo & Zhao, 2018). Adaptive meshes are helpful in achieving desired results at a faster rate.

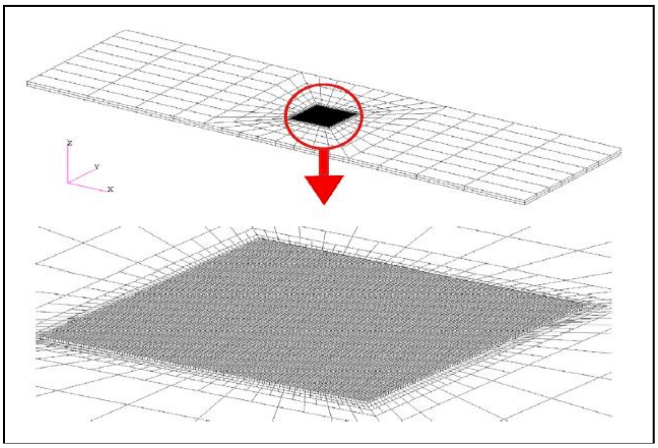

Figure IV.8 Example of FEM adaptive mesh (Denlinger et al., 2017)

The mesh domain dimensions used in the model are shown in Figure IV.9. The total diameter of the powder bed domain is 4mm, and the thickness is 1mm. The ZnSe window is also considered with the same diameter and a thickness of 1.5mm. The material properties of ZnSe are from the manufacturer and are as follows: thermal conductivity is 18W/mK, density is 5270kg/m^{3,} and specific heat capacity is 339 J/ kgK. An adaptive mesh with a very fine mesh of 100 µm is used in the laser impact area, while a coarse mesh is used in remaining areas. The mesh size used at the centre of the domain is the same as that of the pixel distance in the thermal image from the experiments.

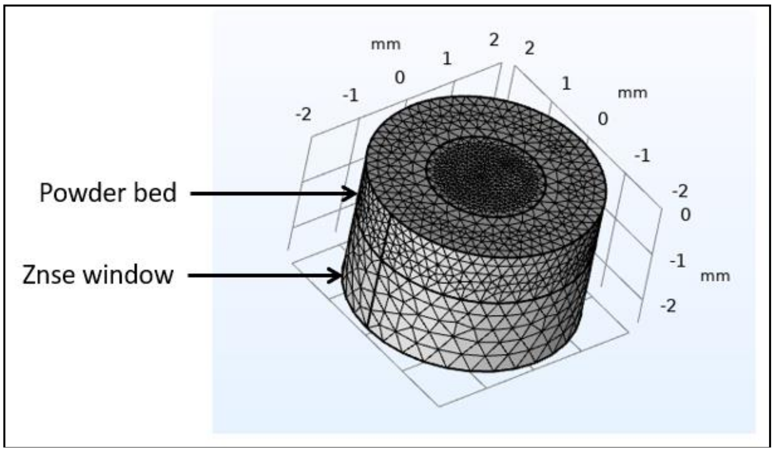

Figure IV.9 Computational Domain with the adaptive mesh. A fine mesh is used in the laser impact area (centre) whereas a coarser mesh is used in the remaining area.

IV.6 Results and discussions

The experimental protocol includes the following steps:
1. Preparation of an uniform powder bed with PA12 CB and PA6 CB;
2. Turning on the stationary laser beam to heat the powder bed for 10s and allowing it to cool down;
3. Simultaneously using the thermal cameras, capturing the temperatures along the powder bed.
The simulations were run for various model parameters, as mentioned in the test matrix above. The boundary conditions include the laser heating for 10s. The initial conditions include the ambient temperature as the room temperature and the heat transfer along the sides of the powder bed are neglected. The model prediction values are compared with the experimental values measured on the powder surface along a longitudinal distance from the centre of the laser spot at lower and higher temperatures at various times, i.e., at time t=1s, the temperature in the powder bed is lower and at time t=10s, it is higher. As a next step, with the laser absorptivity fixed at certain value and the thermal conductivity was modified +/- 10% value from the temperature dependent values (from Figure IV.7) in a way to match the experimental values at various time periods. The liquid melt pool thermal conductivity value calculated from experiments (from section III.9) is also included along with the effective thermal conductivity model. The phase transition temperature was 20°C higher than the melting temperature of the polyamide, at which the powder was assumed completely turned into the liquid phase.

Inspection of plots in Figure IV.10 suggests that for PA12 CB, the k_1A_2 (K_1 thermal conductivity from Figure IV.7 and A_2 absorptivity) correspond to the best fit of experimental profiles, whereas higher absorptivity are increasing the temperatures beyond the experimental values. At higher distances where temperature decays to lower values, the model predictions show a better agreement with the experimental values. Closer to the laser spot where higher temperatures are reached and for longer times, the model is underpredicting the experimental values.

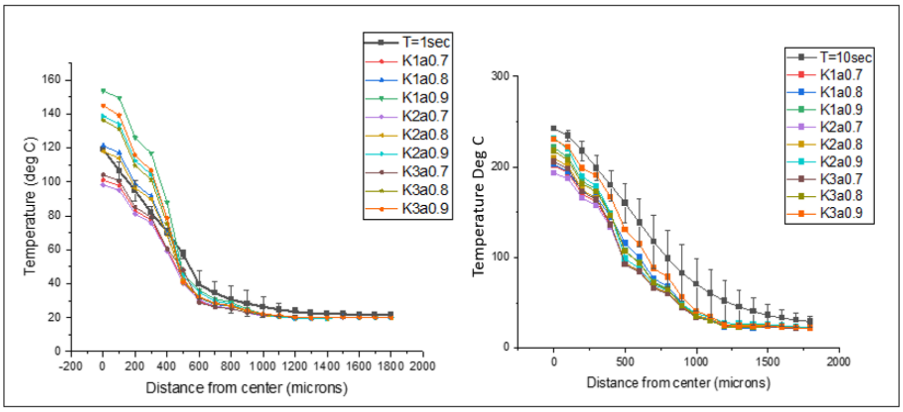

Figure IV.10 Surface temperature vs. distance from centre for PA12 CB: comparison between experimental values and model predictions parametric in laser absorptivity and thermal conductivity values, at t=1 s (left) and at t=10s (right)

As shown in Figure IV.11, the model predictions resulted closer to the experimental values in the lower temperature portion of the profile, whereas it is still underpredicting in the higher temperature zone close to the centre. In Figure IV.12, the data for PA6 CB is shown. The model well predicts the experimental data. However, for both powders, the model underestimates the higher temperature zone. This may be due to the fact that the thermal camera readings could be affected by a higher uncertainty at melting temperatures. In fact, there is no way to include a corresponding emissivity for melt areas in the camera as the thermal camera emissivity settings are fixed (i.e., emissivity variation with temperature cannot be included). A lower emissivity value in the melt pool means a higher temperature measured by the camera.

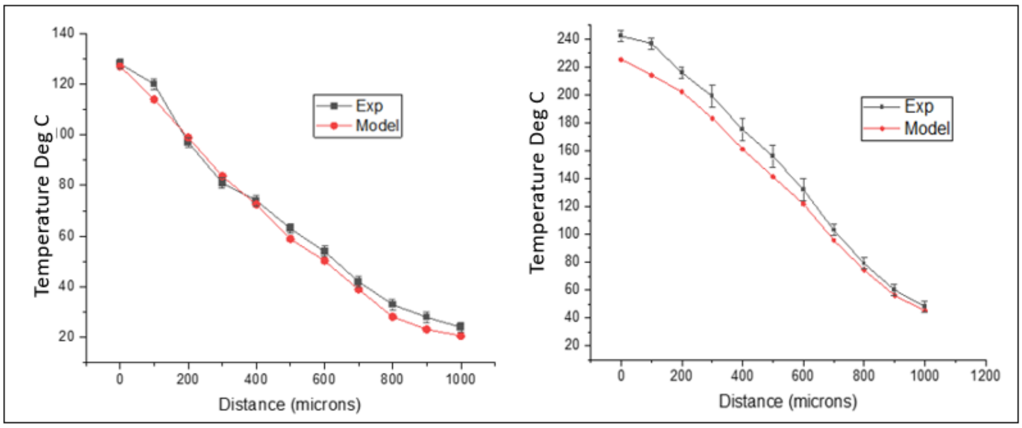

Figure IV.11 Surface temperature vs. distance from centre for PA12 CB: comparison between experimental values and model predictions for laser absorptivity=80/m and thermal conductivity=K1 W/mK values at t=1 s (left) and at t=10s (right)

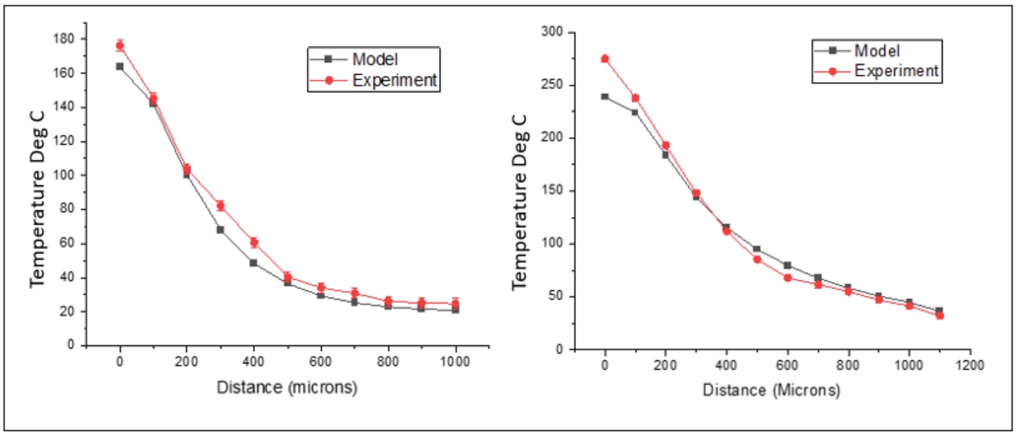

Figure IV.12 Surface temperature vs. distance from centre for PA6 CB: comparison between experimental values and model predictions for laser absorptivity=95/m and thermal conductivity=K1 W/mK values at t=1 s (left) and at t=10s (right)

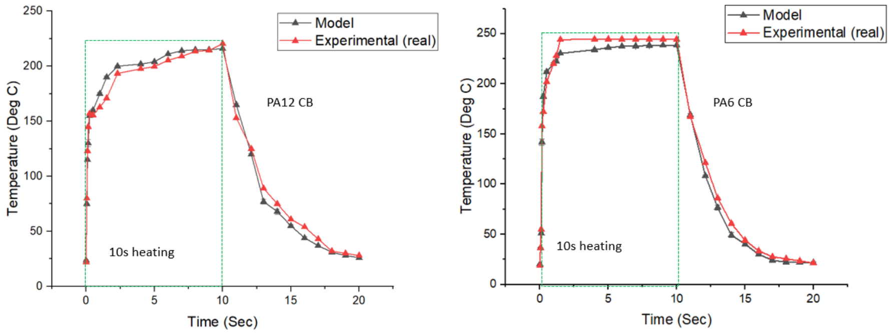

Figure IV.13 Temperature Vs time on the powder surface at laser impact point: comparison between experimental values (temperature compensated for emissivity) and model predictions. PA12 CB (left) and PA6 CB (right)

Figure IV.13 reports temperature variation over the time on the powder surface at laser impact point for both powders.

The relationship to calculate the measured temperature from apparent value is:

$$\varepsilon_{used} = \frac{T_{app}^4 - T_{amb}^4}{T_{meas}^4 - T_{amb}^4} \tag{23}$$

For the real emissivity,

$$\varepsilon_{real} = \frac{T_{app}^4 - T_{amb}^4}{T_{real}^4 - T_{amb}^4} \tag{24}$$

Combining the equations, we get the real temperature,

$$T_{real} = \left[T_{amb}^4 + \frac{\varepsilon_{used}}{\varepsilon_{real}}(T_{meas}^4 - T_{amb}^4)\right]^{1/4} \tag{25}$$

Where, ε_{used} is the used emissivity value in the Optris thermal camera, ε_{real} is the real emissivity value of the melt area, T_{app} is the apparent temperature, T_{real} is the real temperature and T_{meas} is the measured temperature and T_{amb} is the ambient temperature.

In the case of PA12 CB, the laser heating took a few seconds to reach a steady state, whereas in PA6 CB, the laser absorption was much faster. The steady state was achieved at a faster rate as well. Figure IV.14 shows the variation of temperature at a sample point 3 mm away from the laser impact point for both PA12 CB and PA6 CB. As the values are much lower temperatures than the melting point, the model predicts very well. It can be noted that the PA12 CB just reaches steady state at 10s whereas the PA6 CB already reaches steady state midway during the heating. This is due to the faster heating of PA6 CB as noticed in Figure IV.13.

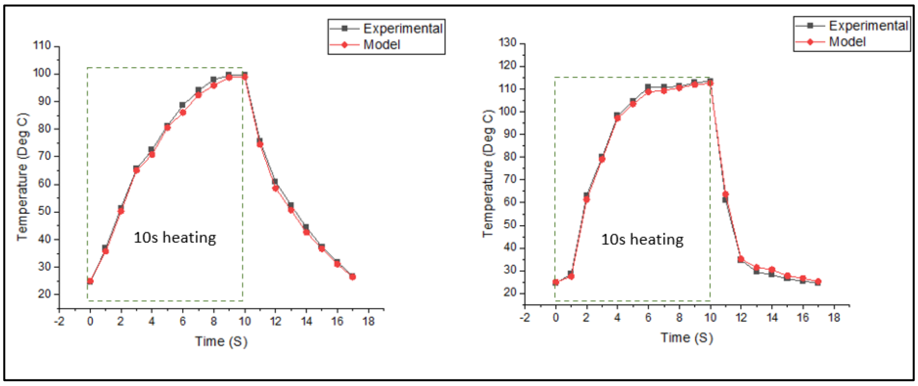

Figure IV.14 Temperature Vs time on the powder surface at a sample 3mm away from the laser impact point: comparison between experimental values and model predictions. PA12 CB (left) and PA6 CB (right)

Model predictions provided also temperature profiles at 1mm below the surface of the powder bed for comparison with the experimental values measured by the SEEK camera (reported in Figure IV.15 left) and with additional experimental data compared with the model at various distances, (reported in Figure IV.15 right). Inspection of Figure IV.15 reveals lower temperatures were achieved at 1mm below the powder surface, which the model predicts well for both powders except for the peak temperature. Similarly, Figure IV.16 shows the corresponding values for PA6 CB.

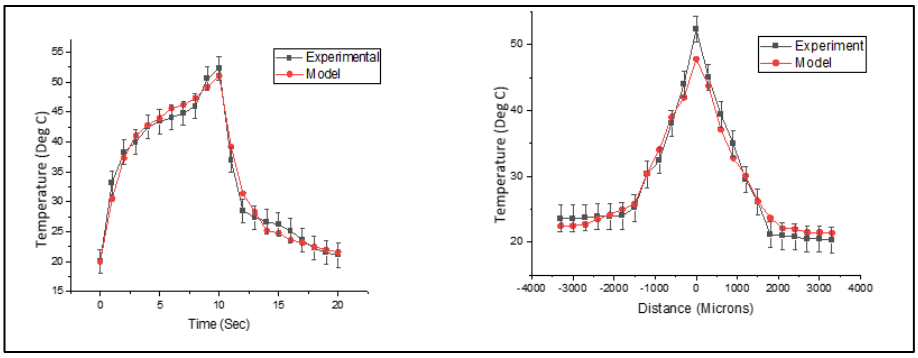

Figure IV.15 Temperature 1mm below the surface for PA12 CB: temperature vs time, SEEK thermal camera data (left) and temperature vs distance from laser impact zone (right)

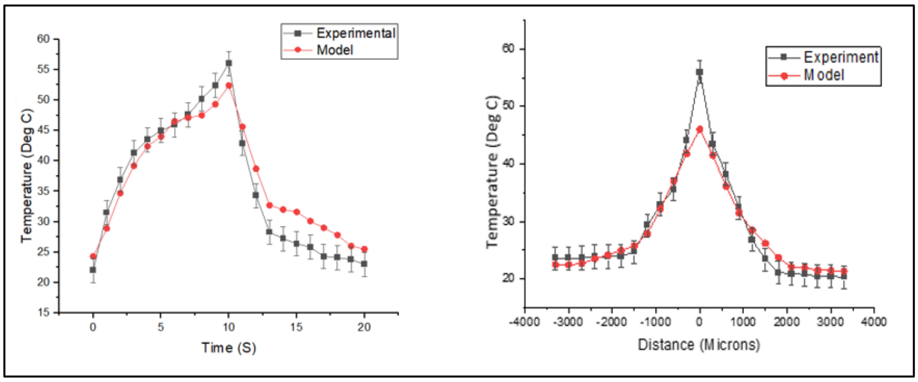

Figure IV.16 Temperature 1mm below the surface for PA6 CB: temperature vs time, SEEK thermal camera data & model comparison (left) and temperature vs distance from laser impact zone (right)

The root mean square error (RMSE) error of the model is given by the equation

$$RMSE = \sqrt{\frac{\Sigma(T_{exp} - T_Q)^2}{N}} \tag{26}$$

Where T_{exp} is the mean experimental temperature of three tests, T_Q is the equivalent model temperature data points, N is the number of temperature data points.

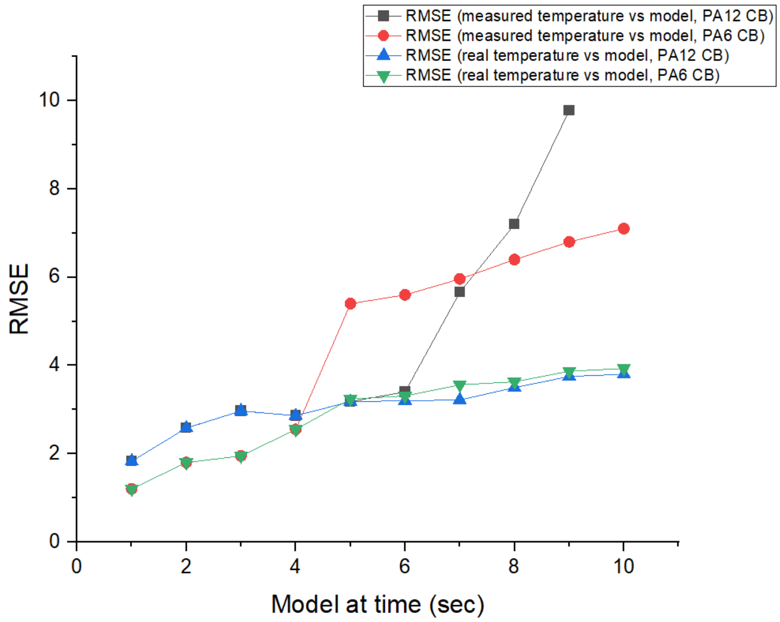

Figure IV.17 RMSE: Experimental vs model for PA12 CB and PA6 CB from t=0s till t=10s of laser heating. The measured apparent temperatures from thermal camera vs model predictions have higher error values at higher temperatures. The real temperatures from thermal camera (after accounting for change in emissivity) has lower error and matches well with model

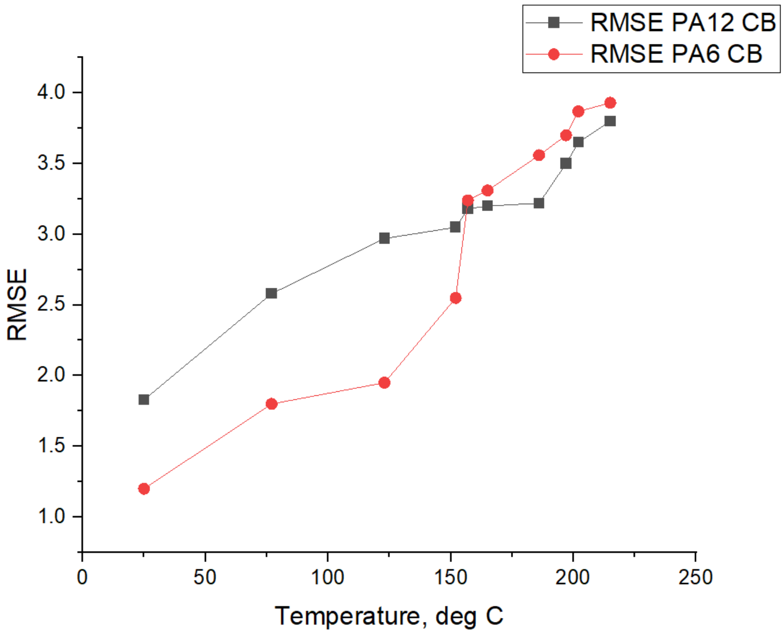

Figure IV.18 RMSE: Experimental vs model for PA12 CB and PA6 CB. Errors are depicted for model vs real experimental values at various temperatures of laser heating

The model predicts the experimental values well and are shown in Figure IV.17. The RMSE between the model and measured apparent temperature from the IR camera, without accounting for change in emissivity at higher melting temperatures, have higher deviation from the model. Whereas, after the thermal camera data is accounted for emissivity variation, the real temperature above melting matches well with model. Similar profile for RMSE vs various temperatures of laser heating can be viewed in Figure IV.18.

Chapter V
Heat transfer in Electrostatic powder coating

This project was undertaken in collaboration with the MATHEGRAM consortium partner Airbus central R&T in Germany during a secondment period.

V.1 Introduction

Being most environmentally friendly coating systems, powder coatings are expanding rapidly in industrial applications. The aerospace industry is rethinking some coating processes, too, to produce more sustainable products. In order to be able to replace some traditional liquid paints with paints containing no Volatile Organic Compounds (VOC), these zeroVOC coatings need to fulfil the stringent requirements of the aerospace industry. Not only the formulation and the chemistry of polymer powder coatings have a strong influence on the final properties of the film, but also the curing conditions. The final coatings are obtained applying the electrostatic spraying technique to polymer powders, generating thin powder films on substrates, and curing the powders either in a conventional oven or under Infrared Radiators (IR) developed specifically for the powder materials. These two curing techniques are compared here. The powder coatings are applied on three different substrates used in the aerospace industry: Aluminium, Titanium and Carbon Fibres Reinforced Plastic (CFRP).
A transient three-dimensional finite element model (FEM) is developed to simulate the curing process of the IR heater and the conventional oven. The temperature-dependent material properties are used in the pre-processing of the model. The final temperature profile on the surface of the coating is compared with the experimental values. For heat sensitive substrates, IR curing shows better results since the process is shorter and the heat absorbed by the substrates is smaller than using a conventional oven. Another advantage of the IR heating is the possibility to tune the heat profile above the substrate.

V.2 Working principle of Electrostatic powder coating

A coating is a covering applied to the surface of a part, which is for the purpose of aesthetic, functional or both. The nature of the part (or the substrate) and the coating material itself can be very different. Electrostatic powder coating (EPC) is the process of electrostatically spraying powders to a grounded substrate which is later cured to form a layer. The electrostatic spray technique was developed by Pieter de Lange in the 1960's. The advantages of such coating are the possibility of achieving very thin layers of coating, less than 100μm thick. Figure V.1 below showcases the working principle of an electrostatic powder coating. Once the substrate is coated, it is then cured under infrared heaters. The project focusses on the latter part of infrared heating of the coated substrate.

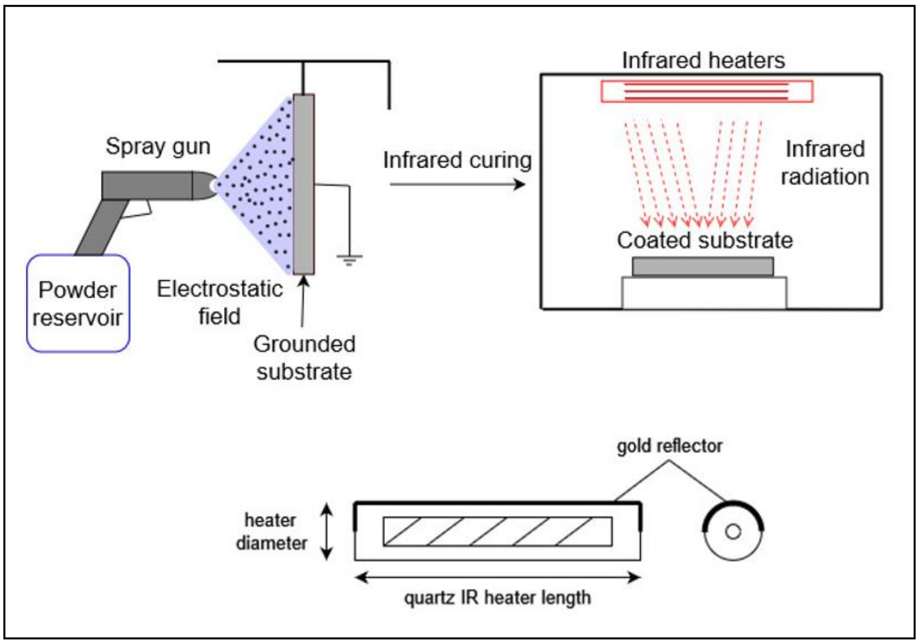

Figure V.1 Working principle of an Electrostatic powder coating (top) and the Infrared heater (bottom)

V.3 State of the art: Electrostatic powder coating

The electrostatic powder coating is divided into three areas : powder charging gun, transportation area and the substrate area, where the deposition and the adhesion occur. The curing is later followed in the process. Bailey (Bailey, 1998) stated that there are three main sorts of acting forces determining the particle motion and particle-substrate deposition behavior: gravity forces, electric forces and aerodynamic forces. This has later been confirmed by Adamiak (Adamiak, 2007b, 2007a) and modelled by Boiger (Boiger, 2016a). To charge electrostatically the particles, two methods exists: corona-charging and tribo-charging. In a standard corona electrostatic spraying system, an airflow laden, with polymer particles with diameters dp comprised between 5 µm and 50 µm, is led past a high voltage electrode and a nozzle. In combination with a grounded substrate of zero potential, the negatively charged electrode causes the formation of an electric potential field, which creates an electric force field between the gun and the substrate. The field lines of the electric field originate from the substrate and enter the electrode (Boiger, 2016b). When it comes to curing, after the parts adhering electrostatically to the substrate, the particles need to melt and cure in order to form a film.

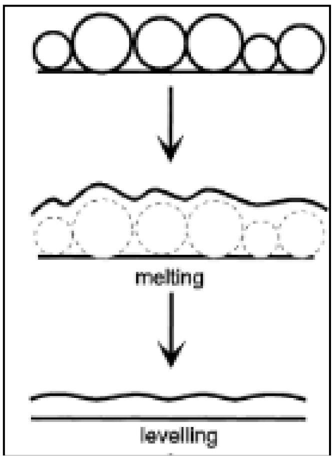

Figure V.2 Powder curing (Ehsani et al., 2009)

The first phase of the film formation consists of melting the particles by heating it. The conventional way to bring heat is to place the sample in an oven at the desired temperature. Another possibility is to use infrared radiators. The former is longer but has the advantage to offer homogeneous heating across the whole part after some time, even for complex-shaped parts. The latter is widely used in continuous line since the time to heat the particles is shorter: approximately 60 s. This stage is crucial to obtain good film quality since the film formation of powder coatings occur in the molten phase. During the film formation and curing, the time-temperature parameters of the process play a major role in the obtention of a good coating. Not only the coating appearance is affected by this stage, but also the mechanical properties of the film.

V.4 Material and methods

The substrate chosen is Al2024 aluminium alloy, one of the widely used in the aerospace industry. The substrate is cut into desired shapes and thickness. The alloy is pretreated with TSA (Tartaric Sulphuric acid Anodising) and being a metal, the electrical conductivity of the substrate is good for electrostatic adhesion of powder particles. The powder used is a hybrid epoxy/polyester. The main advantages of polyester are that it has a relatively low cure temperature and a very good resistance to UV. However, polyester resins are viscous and tend to produce films with an orange-peel effect.

The main advantages of epoxy are the very good resistance to chemicals, the best mechanical properties and a better flowability than polyester. In order to take the best out of these two binders, hybrid epoxy/polyester have been developed. The curing process is done with the custom made infrared radiators Carbon Infrared Emitters, Heraeus Noblelight GmbH. The distance between the radiators and the substrates is 100 mm.

V.5 Heat transfer model

The process is similar to that of the LPBF in the aspect of heat transfer, just as the major difference is the heat source. The Heraeus IR lamp consists of an inner filament which in turn heats the outer quartz tube, which is filled with argon gas. The Infrared heat input is modelled as radiative heat transfer as:

$$q(r) = \sigma . F . A[\varepsilon_{lamp} T_{lamp}^4 - \varepsilon_{coating} T_{coating}^4] \quad (24)$$

where $q(r)$ is the heat radiated from the heater, σ is Stefan Boltzmann's constant, F is the view factor, A surface area of the heater, ε_{lamp} and $\varepsilon_{coating}$ are emissivity of the lamp and coating, respectively, and T_{lamp} and $T_{coating}$ are the temperatures of the lamp and coating, respectively. Identifying the temperature of the lamp is important, and the formula is given by (Labeas et al., 2008):

$$P = \varepsilon_{fil}(T_{fil}) S_{fil} \sigma T_{fil}^4 - 2\pi L_q k_{argon}(T^*) \frac{T_{fil} - T_q}{\ln\left(\frac{d_q}{d_{fil}}\right)} \quad (27)$$

$$\alpha_q(T_{fil}) \varepsilon_{fil}(T_{fil}) S_{fil} \sigma T_{fil}^4 + 2\pi L_q k_{argon}(T^*) \frac{T_{fil} - T_q}{\ln\left(\frac{d_q}{d_{fil}}\right)} = \varepsilon_q S_q \sigma T_q^4 - S_q(T_q - T) \quad (28)$$

where P is the power of the heater, ε_{fil} is the emissivity of the filament (equal to 0.18) , T_{fil} is the temperature of the filament, S_{fil} is the surface area of the

filament (equal to 0.044m^2), α_q is the absorptivity of the quartz (equal to 0.8), L_q is the length of the quartz element (equal to 0.6m) , k_{argon} is the thermal conductivity of argon gas (0.018 W/mK) , $T^* = \frac{T_{fil}+T_q}{2}$, d_q is the diameter of the quartz (0.02m), d_{fil} is the diameter of the filament (0.004m), ε_q is the emissivity of the quartz (0.9), S_q is the surface area of the quartz, T_q is the temperature of the quartz and T is the ambient temperature.
For a given operating power of 1800W, by solving above two nonlinear set of equations the temperature of the lamp is determined equal to 607°C. For six IR heaters with a total input radiosity of 50 W/m^2, the view factor is given as follows:

$$F(view\, factor) = \frac{A_1 F_{L1P} + \cdots + A_6 F_{L6P}}{A_1 + \cdots + A_6} = 0.4674 \tag{29}$$

where A_1 is the area of one IR heater and F_{L1P} is the Lamp to plate view factor, which is given by:

$$F_{LP} = 1 - \sqrt{1 - \left(\frac{D}{S}\right)^2} + \frac{D}{S} tan^{-1} \sqrt{\frac{S^2 - D^2}{D^2}} \tag{30}$$

where D is the diameter and S is the surface area of the heater. The above parameters are given as input to the COMSOL model. An Aluminium substrate is taken, and a polymer-based powder of average particle size distribution of 70µm is used as the coating for the model. The powder thermal conductivity is assumed to be a constant value of 0.1 W/mK, which is in line with the polymer thermal conductivity. The dimensions of the substrate are those of a rectangular plate of 150x100x0.9 mm, and the powder bed thickness is 100 µm. The heaters are 600mm long, and the distance between the heaters is 100 µm, as illustrated in Figure V.3. Conduction, convection and radiation are included in the model.

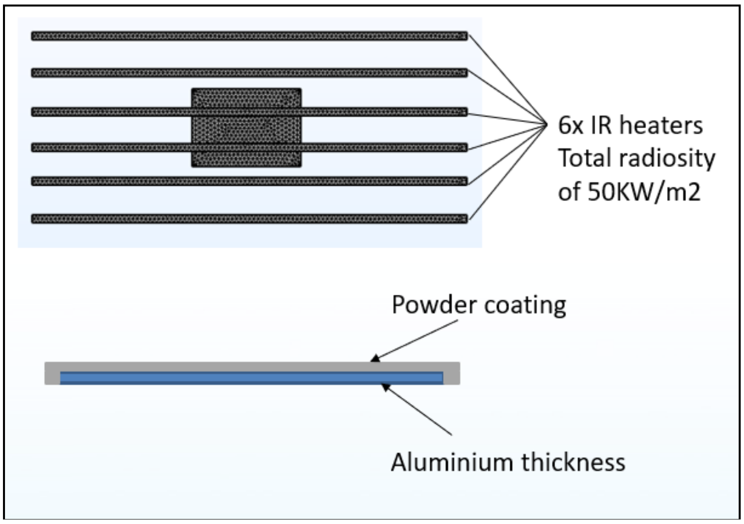

Figure V.3 Six IR heaters heating the substrate (Top) and the powder coated substrate(bottom)

Figure V.4 showcases the finite element-based model results for temperatures at the surface and at the interface of the powder coating. The temperature rises as high as 640°C and reaches steady-state within 90s, which is much higher than the melting temperature of the polymer coating (usually <200°C). A lower IR input power shall be utilised in this case.

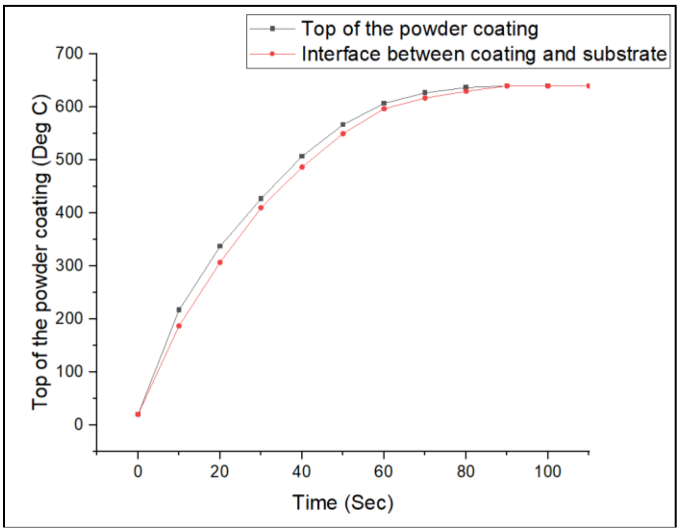

Figure V.4 Heat transfer in electrostatic powder coating curing process. Temperature at the top of the coating and 100 µm below (interface between substrate and coating) vs time

Chapter VI
Conclusion

The project involved experimental and numerical modelling of heat transfer in the selective laser sintering of Polyamide 12 and 6 coated with carbon black powder. An infrared thermography-based experimental set-up involving two thermal cameras was constructed to measure the temperature on the surface of the powder bed and also inside a 1mm thick powder bed. The experimental part included two phases.

In the first one, a heated powder bed set-up was made to measure the temperature dependency of the powder bed and thereby calibration of the thermal cameras. Here we measured the emissivity of the powder beds and found to be nearly constant with temperature until the surface is solid. The PA12 CB has an emissivity value of 0.45 and PA6 CB has slightly higher emissivity value of 0.47. In both cases, the melt pool show an emissivity higher than solid bed: for PA12 CB was 0.85 and for PA6 CB was 0.88. This influences the cooling behaviour of the powder bed; PA6 CB tends to cool down faster than PA12 CB.

The second phase included reassembling the thermal cameras to measure the powder bed's laser-induced temperature rise and cooling down. The experiments were supported by a three-dimensional finite element model considering conductive, convective, and radiative heat transfer and phase change. The challenge lies in the accurate estimation of the material properties such as thermal conductivity, laser absorptivity, powder bed density and specific heat capacity. The model also includes the emissivity at various temperatures. It was found that the temperature-dependent thermal conductivity of the powder bed and that of the melt pool, and also the laser absorptivity are sensitive parameters. A two-particle model with coating methodology was implemented to estimate the powder bed thermal conductivity, including all modes of heat transfer. The thermal conductivities of both powders, in both phase state (powder bed and melt pool) were estimated theoretically and experimentally respectively. The PA6 CB has a much higher thermal conductivity than PA12 CB, which is evident from the faster cooling of the powder bed. A statistical study using the Design of Experiments (DoE) method was performed to evaluate the uncertain material properties. It was found that the PA6 CB has a higher absorptivity of 0.95/m than the PA12 CB which is at 0.8/m. This leads to higher heat absorption and rapid temperature raise in the PA6 CB and therefore the system reaching steady state at much faster rate. The model's accuracy is validated by comparing the temperature data along xyz directions with the experimental values. The model assumed a linear thermal conductivity up until the melting point. The predicted results adhered to the experimental values at lower temperatures, whereas the model has far deviated at elevated temperatures. A nonlinear thermal conductivity might solve the problem. Also, it was understood that the actual experimental laser heat input in the powder bed is not symmetric and includes skewness. Instead, the model heat input assumes a perfect gaussian profile which is not the actual case. The model adheres to the experiments very well in the case of the temperature data at 1mm below the surface.

As part of the secondment, a project on heat transfer in electrostatic powder coating was undertaken. Firsthand, a finite-element-based numerical model was developed to understand the time taken for the curing of the coated substrates. Further experimental data is required to support the accuracy of the model.

VI.1 Future activities

As a next step, a different laser input model will be used in the FEM model. The absorption coefficient of PA12 CB needs to be verified experimentally. Based on the temperature data along the depth, artefacts can be manufactured using an SLS machine, and mechanical characterization can be performed on those parts. Furthermore, a relationship between the temperatures at various depths of the powder bed and the tensile strength of the sintered specimen shall be established as the next step.

Chapter VII
Bibliography

Adamiak, K. (2007a). Numerical investigation of powder trajectories and deposition in tribo-charge powder coating. *IEEE Transactions on Industry Applications*.

Adamiak, K. (2007b). Numerical modeling of tribo-charge powder coating systems. *Journal of Electrostatics*.

Alldredge, J., Slotwinski, J., Storck, S., Kim, S., Goldberg, A., & Montalbano, T. (2018). In-Situ monitoring and modeling of metal additive manufacturing powder bed fusion. *AIP Conference Proceedings*. https://doi.org/10.1063/1.5031504

Ammer, R., Markl, M., Ljungblad, U., Körner, C., & Rüde, U. (2014). Simulating fast electron beam melting with a parallel thermal free surface lattice Boltzmann method. *Computers and Mathematics with Applications*. https://doi.org/10.1016/j.camwa.2013.10.001

Antony, K., Arivazhagan, N., & Senthilkumaran, K. (2014). Numerical and experimental investigations on laser melting of stainless steel 316L metal powders. *Journal of Manufacturing Processes*. https://doi.org/10.1016/j.jmapro.2014.04.001

Bai, J., Goodridge, R. D., Yuan, S., Zhou, K., Chua, C. K., & Wei, J. (2015). Thermal influence of CNT on the polyamide 12 nanocomposite for selective laser sintering. *Molecules*. https://doi.org/10.3390/molecules201019041

Bai, P. K., Cheng, J., Liu, B., & Wang, W. F. (2006). Numerical simulation of temperature field during selective laser sintering of polymer-coated molybdenum powder. *Transactions of Nonferrous Metals Society of China (English Edition)*. https://doi.org/10.1016/S1003-6326(06)60264-1

Bailey, A. G. (1998). *The science and technology of electrostatic powder spraying , transport and coating*. *45*, 85–120.

Bauereiß, A., Scharowsky, T., & Körner, C. (2014). Defect generation and propagation mechanism during additive manufacturing by selective beam melting. *Journal of Materials Processing Technology*. https://doi.org/10.1016/j.jmatprotec.2014.05.002

Bayle, F., & Doubenskaia, M. (2008). *<title>Selective laser melting process monitoring with high speed infra-red camera and pyrometer</title>*. https://doi.org/10.1117/12.786940

Beyaz, R., Ekinci, A., Yurtbasi, Z., Oksuz, M., Ates, M., & Aydin, I. (2022). Thermal, electrical and mechanical properties of carbon fiber/copper powder/carbon black reinforced hybrid Polyamide 6,6 composites.

High Performance Polymers, *0*(0), 1–12. https://doi.org/10.1177/09540083221114752

Boiger, G. (2016a). Characterization of Particle Motion and Deposition Behaviour in Electro-Static Fields. *International Journal of Multiphysics*, *10*(2).

Boiger, G. (2016b). Euler-Lagrangian Model of Particle Motion and Deposition Effects in Electro- Static Fields based on OpenFoam. *International Journal of Multiphysics*, *10*(2), 18.

Boillat, E., Kolossov, S., Glardon, R., Loher, M., Saladin, D., & Levy, G. (2004). Finite element and neural network models for process optimization in selective laser sintering. *Proceedings of the Institution of Mechanical Engineers, Part B: Journal of Engineering Manufacture*. https://doi.org/10.1243/0954405041167121

Boivineau, M., Cagran, C., Doytier, D., Eyraud, V., Nadal, M. H., Wilthan, B., & Pottlacher, G. (2006). Thermophysical properties of solid and liquid Ti-6Al-4V (TA6V) alloy. *International Journal of Thermophysics*. https://doi.org/10.1007/PL00021868

Bugeda, G., Cervera, M., & Lombera, G. (1999). Numerical prediction of temperature and density distributions in selective laser sintering processes. *Rapid Prototyping Journal*. https://doi.org/10.1108/13552549910251846

Carter, L. N., Martin, C., Withers, P. J., & Attallah, M. M. (2014). The influence of the laser scan strategy on grain structure and cracking behaviour in SLM powder-bed fabricated nickel superalloy. *Journal of Alloys and Compounds*. https://doi.org/10.1016/j.jallcom.2014.06.172

Chen, T., & Zhang, Y. (2007). Thermal modeling of laser sintering of two-component metal powder on top of sintered layers via multi-line scanning. *Applied Physics A: Materials Science and Processing*. https://doi.org/10.1007/s00339-006-3739-1

Cheng, B., & Chou, K. (2020). Melt pool evolution study in selective laser melting. *Proceedings - 26th Annual International Solid Freeform Fabrication Symposium - An Additive Manufacturing Conference, SFF 2015*.

Clijsters, S., Craeghs, T., Buls, S., Kempen, K., & Kruth, J. P. (2014). In situ quality control of the selective laser melting process using a high-speed, real-time melt pool monitoring system. *International Journal of Advanced Manufacturing Technology*. https://doi.org/10.1007/s00170-014-6214-8

Contuzzi, N., Campanelli, S. L., & Ludovico, A. D. (2011). 3D finite element analysis in the Selective Laser Melting process. *International Journal of Simulation Modelling*. https://doi.org/10.2507/IJSIMM10(3)1.169

Craeghs, T., Bechmann, F., Berumen, S., & Kruth, J. P. (2010). Feedback control of Layerwise Laser Melting using optical sensors. *Physics*

Procedia. https://doi.org/10.1016/j.phpro.2010.08.078
Craeghs, T., Clijsters, S., Kruth, J. P., Bechmann, F., & Ebert, M. C. (2012). Detection of Process Failures in Layerwise Laser Melting with Optical Process Monitoring. *Physics Procedia*. https://doi.org/10.1016/j.phpro.2012.10.097
Cundall, P. A., & Strack, O. D. L. (1979). A discrete numerical model for granular assemblies. *Géotechnique*, *29*(1), 47–65. https://doi.org/10.1680/geot.1979.29.1.47
Dayal, R., & Gambaryan-Roisman, T. (2017). Heat transfer in granular medium for application to selective laser melting: A numerical study. *International Journal of Thermal Sciences*. https://doi.org/10.1016/j.ijthermalsci.2016.11.014
Delgado, J., Ciurana, J., & Rodríguez, C. A. (2012). Influence of process parameters on part quality and mechanical properties for DMLS and SLM with iron-based materials. *International Journal of Advanced Manufacturing Technology*. https://doi.org/10.1007/s00170-011-3643-5
Dinwiddie, R. B., Kirka, M. M., Lloyd, P. D., Dehoff, R. R., Lowe, L. E., & Marlow, G. S. (2016). Calibrating IR cameras for in-situ temperature measurement during the electron beam melt processing of Inconel 718 and Ti-Al6-V4. *Thermosense: Thermal Infrared Applications XXXVIII*. https://doi.org/10.1117/12.2229070
Doubenskaia, M. A., Zhirnov, I. V., Teleshevskiy, V. I., Bertrand, P., & Smurov, I. Y. (2015). Determination of true temperature in selective laser melting of metal powder using infrared camera. *Materials Science Forum*. https://doi.org/10.4028/www.scientific.net/MSF.834.93
Dowling, L., Kennedy, J., O'Shaughnessy, S., & Trimble, D. (2020). A review of critical repeatability and reproducibility issues in powder bed fusion. *Materials and Design*, *186*, 108346. https://doi.org/10.1016/j.matdes.2019.108346
Edwards, P., O'Conner, A., & Ramulu, M. (2013). Electron beam additive manufacturing of titanium components: Properties and performance. *Journal of Manufacturing Science and Engineering, Transactions of the ASME*. https://doi.org/10.1115/1.4025773
Ehsani, M., Yousefi, A. A., & Yeganeh, S. S. (2009). Study of rheological behaviours of electrostatic thermoset powder coatings. *E-Polymers*, *December*. https://doi.org/10.1515/epoly.2009.9.1.1667
Esfahani, M. N., Bian, L., & Tian, W. (2019). *IN-SITU LAYER-WISE QUALITY MONITORING FOR LASER-BASED ADDITIVE MANUFACTURING USING IMAGE SERIES ANALYSIS*. 202–212.
Espera, A. H., Valino, A. D., Palaganas, J. O., Souza, L., Chen, Q., & Advincula, R. C. (2019). 3D Printing of a Robust Polyamide-12-Carbon Black Composite via Selective Laser Sintering: Thermal and

Electrical Conductivity. *Macromolecular Materials and Engineering*, *304*(4). https://doi.org/10.1002/mame.201800718
Fischer, P., Locher, M., Romano, V., Weber, H. P., Kolossov, S., & Glardon, R. (2004). Temperature measurements during selective laser sintering of titanium powder. *International Journal of Machine Tools and Manufacture*. https://doi.org/10.1016/j.ijmachtools.2004.04.019
Foroozmehr, A., Badrossamay, M., Foroozmehr, E., & Golabi, S. (2016). Finite Element Simulation of Selective Laser Melting process considering Optical Penetration Depth of laser in powder bed. *Materials and Design*. https://doi.org/10.1016/j.matdes.2015.10.002
Foster, B. K., Reutzel, E. W., Nassar, A. R., Dickman, C. J., & Hall, B. T. (2015). A brief survey of sensing for metal-based powder bed fusion additive manufacturing. *Dimensional Optical Metrology and Inspection for Practical Applications IV*. https://doi.org/10.1117/12.2180654
Fürstenau, J. P., Wessels, H., Weißenfels, C., & Wriggers, P. (2020). Generating virtual process maps of SLM using powder-scale SPH simulations. *Computational Particle Mechanics*. https://doi.org/10.1007/s40571-019-00296-3
Gao, Y., Xing, J., Zhang, J., Luo, N., & Zheng, H. (2008). Research on measurement method of selective laser sintering (SLS) transient temperature. *Optik*. https://doi.org/10.1016/j.ijleo.2007.01.010
Gobal, A., & Ravani, B. (2017). Physical modeling for selective laser sintering process. *Journal of Computing and Information Science in Engineering*. https://doi.org/10.1115/1.4034473
Gong, X., Cheng, B., Price, S., & Chou, K. (2013). Powder-bed electron-beam-melting additive manufacturing: powder characterization, process simulation and metrology. *Early Career Technical Conference, Birmingham, AL*.
Grasso, M., & Colosimo, B. M. (2017). Process defects and in situ monitoring methods in metal powder bed fusion: A review. In *Measurement Science and Technology*. https://doi.org/10.1088/1361-6501/aa5c4f
Grasso, M., Laguzza, V., Semeraro, Q., & Colosimo, B. M. (2017). In-Process Monitoring of Selective Laser Melting: Spatial Detection of Defects Via Image Data Analysis. *Journal of Manufacturing Science and Engineering, Transactions of the ASME*. https://doi.org/10.1115/1.4034715
Hagen, D., Chen, A., Beaman, J. J., & Kovar, D. (2019). *Moisture Effects on Selective Laser Flash Sintering of Yttria-Stabilized Zirconia*. 873–891.
Harrison, N. J., Todd, I., & Mumtaz, K. (2015). Reduction of micro-cracking in nickel superalloys processed by Selective Laser Melting: A fundamental alloy design approach. *Acta Materialia*. https://doi.org/10.1016/j.actamat.2015.04.035
Ho, H. C. H., Cheung, W. L., & Gibson, I. (2002). Effects of graphite

powder on the laser sintering behaviour of polycarbonate. *Rapid Prototyping Journal*. https://doi.org/10.1108/13552540210441148

Hooper, P. A. (2018). Melt pool temperature and cooling rates in laser powder bed fusion. *Additive Manufacturing*. https://doi.org/10.1016/j.addma.2018.05.032

Hu, D., & Kovacevic, R. (2003). Modelling and measuring the thermal behaviour of the molten pool in closed-loop controlled laser-based additive manufacturing. *Proceedings of the Institution of Mechanical Engineers, Part B: Journal of Engineering Manufacture*. https://doi.org/10.1243/095440503321628125

Hussein, A., Hao, L., Yan, C., & Everson, R. (2013). Finite element simulation of the temperature and stress fields in single layers built without-support in selective laser melting. *Materials and Design*. https://doi.org/10.1016/j.matdes.2013.05.070

Islam, M., Purtonen, T., Piili, H., Salminen, A., & Nyrhilä, O. (2013). Temperature profile and imaging analysis of laser additive manufacturing of stainless steel. *Physics Procedia*. https://doi.org/10.1016/j.phpro.2013.03.156

Kanko, J. A., Sibley, A. P., & Fraser, J. M. (2016). In situ morphology-based defect detection of selective laser melting through inline coherent imaging. *Journal of Materials Processing Technology*. https://doi.org/10.1016/j.jmatprotec.2015.12.024

Karayagiz, K., Elwany, A., Tapia, G., Franco, B., Johnson, L., Ma, J., Karaman, I., & Arróyave, R. (2019). Numerical and experimental analysis of heat distribution in the laser powder bed fusion of Ti-6Al-4V. *IISE Transactions*. https://doi.org/10.1080/24725854.2018.1461964

Khairallah, S. A., & Anderson, A. (2014). Mesoscopic simulation model of selective laser melting of stainless steel powder. *Journal of Materials Processing Technology*. https://doi.org/10.1016/j.jmatprotec.2014.06.001

Kleszczynski, S., Zur Jacobsmühlen, J., Sehrt, J. T., & Witt, G. (2012). Error detection in laser beam melting systems by high resolution imaging. *23rd Annual International Solid Freeform Fabrication Symposium - An Additive Manufacturing Conference, SFF 2012*.

Kolossov, S., Boillat, E., Glardon, R., Fischer, P., & Locher, M. (2004). 3D FE simulation for temperature evolution in the selective laser sintering process. *International Journal of Machine Tools and Manufacture*. https://doi.org/10.1016/j.ijmachtools.2003.10.019

Krauss, H., Eschey, C., & Zaeh, M. F. (2012). Thermography for monitoring the selective laser melting process. *23rd Annual International Solid Freeform Fabrication Symposium - An Additive Manufacturing Conference, SFF 2012*.

Krol, T. A., Seidel, C., Schilp, J., Hofmann, M., Gan, W., & Zaeh, M. F. (2013). Verification of structural simulation results of metal-based additive manufacturing by means of neutron diffraction. *Physics Procedia*. https://doi.org/10.1016/j.phpro.2013.03.158

Kruth, J. P., Froyen, L., Van Vaerenbergh, J., Mercelis, P., Rombouts, M., & Lauwers, B. (2004). Selective laser melting of iron-based powder. *Journal of Materials Processing Technology*. https://doi.org/10.1016/j.jmatprotec.2003.11.051

Kruth, J. P., Mercelis, P., Van Vaerenbergh, J., Froyen, L., & Rombouts, M. (2005). Binding mechanisms in selective laser sintering and selective laser melting. In *Rapid Prototyping Journal*. https://doi.org/10.1108/13552540510573365

Labeas, G. N., Watiti, V. B., & Katsiropoulos, C. V. (2008). Thermomechanical simulation of infrared heating diaphragm forming process for thermoplastic parts. *Journal of Thermoplastic Composite Materials*, *21*(4), 353–370. https://doi.org/10.1177/0892705708089480

Lane, B., Moylan, S., Whitenton, E. P., & Ma, L. (2016). Thermographic measurements of the commercial laser powder bed fusion process at NIST. *Rapid Prototyping Journal*. https://doi.org/10.1108/RPJ-11-2015-0161

Li, R., Liu, J., Shi, Y., Wang, L., & Jiang, W. (2012). Balling behavior of stainless steel and nickel powder during selective laser melting process. *International Journal of Advanced Manufacturing Technology*. https://doi.org/10.1007/s00170-011-3566-1

Li, Y., & Gu, D. (2014). Parametric analysis of thermal behavior during selective laser melting additive manufacturing of aluminum alloy powder. *Materials and Design*. https://doi.org/10.1016/j.matdes.2014.07.006

Liu, B., Wildman, R., Tuck, C., Ashcroft, I., & Hague, R. (2011). Investigaztion the effect of particle size distribution on processing parameters optimisation in selective laser melting process. *22nd Annual International Solid Freeform Fabrication Symposium - An Additive Manufacturing Conference, SFF 2011*.

Liu, F. R., Zhang, Q., Zhou, W. P., Zhao, J. J., & Chen, J. M. (2012). Micro scale 3D FEM simulation on thermal evolution within the porous structure in selective laser sintering. *Journal of Materials Processing Technology*. https://doi.org/10.1016/j.jmatprotec.2012.05.010

Lott, P., Schleifenbaum, H., Meiners, W., Wissenbach, K., Hinke, C., & Bültmann, J. (2011). Design of an optical system for the in situ process monitoring of Selective Laser Melting (SLM). *Physics Procedia*. https://doi.org/10.1016/j.phpro.2011.03.085

Luding, S. (2008). Cohesive, frictional powders: Contact models for tension. *Granular Matter*. https://doi.org/10.1007/s10035-008-0099-x

Luo, Z., & Zhao, Y. (2018). A survey of finite element analysis of temperature and thermal stress fields in powder bed fusion Additive Manufacturing. In *Additive Manufacturing*. https://doi.org/10.1016/j.addma.2018.03.022

M'Saoubi, R., & Chandrasekaran, H. (2004). Investigation of the effects of tool micro-geometry and coating on tool temperature during orthogonal turning of quenched and tempered steel. *International Journal of Machine Tools and Manufacture*. https://doi.org/10.1016/j.ijmachtools.2003.10.006

Madenci, E., & Guven, I. (2006). The finite element method and applications in engineering using Ansys®. In *The Finite Element Method and Applications in Engineering Using Ansys®*. https://doi.org/10.1007/978-0-387-28290-9

Mani, M., Feng, S., Lane, B., Donmez, A., Moylan, S., & Fesperman, R. (2017). Measurement science needs for real-time control of additive manufacturing powder-bed fusion processes. In *Additive Manufacturing Handbook: Product Development for the Defense Industry*. https://doi.org/10.1201/9781315119106

Markl, M., & Körner, C. (2018). Powder layer deposition algorithm for additive manufacturing simulations. *Powder Technology*. https://doi.org/10.1016/j.powtec.2018.02.026

Masubuchi, K., & Agapakis, J. (1982). *ANALYSIS AND CONTROL OF RESIDUAL STRESSES, DISTORTION AND THEIR CONSEQUENCES IN WELDED STRUCTURES.*

Matsumoto, M., Shiomi, M., Osakada, K., & Abe, F. (2002). Finite element analysis of single layer forming on metallic powder bed in rapid prototyping by selective laser processing. *International Journal of Machine Tools and Manufacture*. https://doi.org/10.1016/S0890-6955(01)00093-1

Meier, C., Penny, R. W., Zou, Y., Gibbs, J. S., & Hart, A. J. (2018). THERMOPHYSICAL PHENOMENA IN METAL ADDITIVE MANUFACTURING BY SELECTIVE LASER MELTING: FUNDAMENTALS, MODELING, SIMULATION, AND EXPERIMENTATION. *Annual Review of Heat Transfer*. https://doi.org/10.1615/annualrevheattransfer.2018019042

Mercelis, P., & Kruth, J. P. (2006). Residual stresses in selective laser sintering and selective laser melting. *Rapid Prototyping Journal*. https://doi.org/10.1108/13552540610707013

Mireles, J., Ridwan, S., Morton, P. A., Hinojos, A., & Wicker, R. B. (2015). Analysis and correction of defects within parts fabricated using powder bed fusion technology. *Surface Topography: Metrology and Properties*. https://doi.org/10.1088/2051-672X/3/3/034002

Mishra, B. K., & Rajamani, R. K. (1992). The discrete element method for the simulation of ball mills. *Applied Mathematical Modelling*.

https://doi.org/10.1016/0307-904X(92)90035-2
Mokrane, A., Boutaous, M., & Xin, S. (2018). Process of selective laser sintering of polymer powders: Modeling, simulation, and validation. In *Comptes Rendus - Mecanique*. https://doi.org/10.1016/j.crme.2018.08.002
Mousa, A. A. (2016). Experimental investigations of curling phenomenon in selective laser sintering process. *Rapid Prototyping Journal*. https://doi.org/10.1108/RPJ-12-2013-0132
Moylan, S., Drescher, J., & Donmez, M. A. (2014). Powder bed fusion machine performance testing. *Proceedings - ASPE 2014 Spring Topical Meeting: Dimensional Accuracy and Surface Finish in Additive Manufacturing*.
Panwisawas, C., Qiu, C., Anderson, M. J., Sovani, Y., Turner, R. P., Attallah, M. M., Brooks, J. W., & Basoalto, H. C. (2017). Mesoscale modelling of selective laser melting: Thermal fluid dynamics and microstructural evolution. *Computational Materials Science*. https://doi.org/10.1016/j.commatsci.2016.10.011
Parthasarathy, V. N., & Kodiyalam, S. (1991). A constrained optimization approach to finite element mesh smoothing. *Finite Elements in Analysis and Design*. https://doi.org/10.1016/0168-874X(91)90004-I
Patil, R. B., & Yadava, V. (2007). Finite element analysis of temperature distribution in single metallic powder layer during metal laser sintering. *International Journal of Machine Tools and Manufacture*. https://doi.org/10.1016/j.ijmachtools.2006.09.025
Pereira, T., Kennedy, J. V., & Potgieter, J. (2019). A comparison of traditional manufacturing vs additive manufacturing, the best method for the job. *Procedia Manufacturing*. https://doi.org/10.1016/j.promfg.2019.02.003
Price, S., Cooper, K., & Chou, K. (2012). Evaluations of temperature measurements by near-infrared thermography in powder-based electron-beam additive manufacturing. *23rd Annual International Solid Freeform Fabrication Symposium - An Additive Manufacturing Conference, SFF 2012*.
Ridwan, T., & Keck, R. W. (2014). AUTOMATIC LAYERWISE ACQUISITION OF THERMAL AND GEOMETRIC DATA OF THE ELECTRON BEAM MELTING PROCESS USING INFRARED. *Solid Freeform Fabrication Proceedings*.
Roberts, I. A., Wang, C. J., Esterlein, R., Stanford, M., & Mynors, D. J. (2009). A three-dimensional finite element analysis of the temperature field during laser melting of metal powders in additive layer manufacturing. *International Journal of Machine Tools and Manufacture*. https://doi.org/10.1016/j.ijmachtools.2009.07.004
Rodriguez, E., Mireles, J., Terrazas, C. A., Espalin, D., Perez, M. A., & Wicker, R. B. (2015). Approximation of absolute surface temperature

measurements of powder bed fusion additive manufacturing technology using in situ infrared thermography. *Additive Manufacturing*. https://doi.org/10.1016/j.addma.2014.12.001
Sames, W. J., List, F. A., Pannala, S., Dehoff, R. R., & Babu, S. S. (2016). The metallurgy and processing science of metal additive manufacturing. In *International Materials Reviews*. https://doi.org/10.1080/09506608.2015.1116649
Santospirito, S. P., Słyk, K., Luo, B., Łopatka, R., Gilmour, O., & Rudlin, J. (2013). Detection of defects in laser powder deposition (LPD) components by pulsed laser transient thermography. *Thermosense: Thermal Infrared Applications XXXV*. https://doi.org/10.1117/12.2016139
Schoinochoritis, B., Chantzis, D., & Salonitis, K. (2017). Simulation of metallic powder bed additive manufacturing processes with the finite element method: A critical review. In *Proceedings of the Institution of Mechanical Engineers, Part B: Journal of Engineering Manufacture*. https://doi.org/10.1177/0954405414567522
Shapiro, M., Dudko, V., Royzen, V., Krichevets, Y., Lekhtmakher, S., Grozubinsky, V., Shapira, M., & Brill, M. (2004). Characterization of Powder Beds by Thermal Conductivity: Effect of Gas Pressure on the Thermal Resistance of Particle Contact Points. *Particle and Particle Systems Characterization*. https://doi.org/10.1002/ppsc.200400943
Sharratt, B. M. (2015). Non-Destructive Techniques and Technologies for Qualification of Additive Manufactured Parts and Processes: A Literature Review. *Department of National Defence of Canada*.
Shen, N., & Chou, K. (2012). Thermal modeling of electron beam additive manufacturing process - Powder sintering effects. *ASME 2012 International Manufacturing Science and Engineering Conference Collocated with the 40th North American Manufacturing Research Conference and in Participation with the Int. Conf., MSEC 2012*. https://doi.org/10.1115/MSEC2012-7253
Shiomi, M., Yoshidome, A., Abe, F., & Osakada, K. (1999). Finite element analysis of melting and solidifying processes in laser rapid prototyping of metallic powders. *International Journal of Machine Tools and Manufacture*. https://doi.org/10.1016/S0890-6955(98)00036-4
Slotwinski, J. A., Garboczi, E. J., & Hebenstreit, K. M. (2014). Porosity measurements and analysis for metal additive manufacturing process control. *Journal of Research of the National Institute of Standards and Technology*. https://doi.org/10.6028/jres.119.019
Smith, R. J., Hirsch, M., Patel, R., Li, W., Clare, A. T., & Sharples, S. D. (2016). Spatially resolved acoustic spectroscopy for selective laser melting. *Journal of Materials Processing Technology*. https://doi.org/10.1016/j.jmatprotec.2016.05.005

Sofia, D., Granese, M., Barletta, D., & Poletto, M. (2015). Laser sintering of unimodal distributed glass powders of different size. *Procedia Engineering*. https://doi.org/10.1016/j.proeng.2015.01.180

Song, B., Dong, S., Liao, H., & Coddet, C. (2012). Process parameter selection for selective laser melting of Ti6Al4V based on temperature distribution simulation and experimental sintering. *International Journal of Advanced Manufacturing Technology*. https://doi.org/10.1007/s00170-011-3776-6

Soundararajan, B., Sofia, D., Barletta, D., & Poletto, M. (2021). Review on modeling techniques for powder bed fusion processes based on physical principles. *Additive Manufacturing*, *47*(August), 102336. https://doi.org/10.1016/j.addma.2021.102336

Steuben, J. C., Iliopoulos, A. P., & Michopoulos, J. G. (2016). Discrete element modeling of particle-based additive manufacturing processes. *Computer Methods in Applied Mechanics and Engineering*. https://doi.org/10.1016/j.cma.2016.02.023

Tammas-Williams, S., Zhao, H., Léonard, F., Derguti, F., Todd, I., & Prangnell, P. B. (2015). XCT analysis of the influence of melt strategies on defect population in Ti-6Al-4V components manufactured by Selective Electron Beam Melting. *Materials Characterization*. https://doi.org/10.1016/j.matchar.2015.02.008

Trevisan, S., Wang, W., & Laumert, B. (2021). Coatings utilization to modify the effective properties of high temperature packed bed thermal energy storage. *Applied Thermal Engineering*, *185*. https://doi.org/10.1016/j.applthermaleng.2020.116414

TURNER, M. J., CLOUGH, R. W., MARTIN, H. C., & TOPP, L. J. (1956). Stiffness and Deflection Analysis of Complex Structures. *Journal of the Aeronautical Sciences*. https://doi.org/10.2514/8.3664

Van Belle, L., Vansteenkiste, G., & Boyer, J. C. (2012). Comparisons of numerical modelling of the Selective Laser Melting. *Key Engineering Materials*. https://doi.org/10.4028/www.scientific.net/KEM.504-506.1067

Wegner, A., & Witt, G. (2011). Process monitoring in laser sintering using thermal imaging. *22nd Annual International Solid Freeform Fabrication Symposium - An Additive Manufacturing Conference, SFF 2011*.

Weirather, J., Rozov, V., Wille, M., Schuler, P., Seidel, C., Adams, N. A., & Zaeh, M. F. (2019). A Smoothed Particle Hydrodynamics Model for Laser Beam Melting of Ni-based Alloy 718. *Computers and Mathematics with Applications*. https://doi.org/10.1016/j.camwa.2018.10.020

Williams, R. J., Piglione, A., Rønneberg, T., Jones, C., Pham, M. S., Davies, C. M., & Hooper, P. A. (2019). In situ thermography for laser powder bed fusion: Effects of layer temperature on porosity, microstructure and

mechanical properties. *Additive Manufacturing*. https://doi.org/10.1016/j.addma.2019.100880
Wu, Y. C., San, C. H., Chang, C. H., Lin, H. J., Marwan, R., Baba, S., & Hwang, W. S. (2018). Numerical modeling of melt-pool behavior in selective laser melting with random powder distribution and experimental validation. *Journal of Materials Processing Technology*. https://doi.org/10.1016/j.jmatprotec.2017.11.032
Xin, L., Boutaous, M., Xin, S., & Siginer, D. A. (2017). Numerical modeling of the heating phase of the selective laser sintering process. *International Journal of Thermal Sciences*. https://doi.org/10.1016/j.ijthermalsci.2017.05.017
Yasa, E., Deckers, J., Craeghs, T., Badrossamay, M., & Kruth, J. P. (2009). Investigation on occurrence of elevated edges in selective laser melting. *20th Annual International Solid Freeform Fabrication Symposium, SFF 2009*.
Yin, J., Zhu, H., Ke, L., Lei, W., Dai, C., & Zuo, D. (2012). Simulation of temperature distribution in single metallic powder layer for laser micro-sintering. *Computational Materials Science*. https://doi.org/10.1016/j.commatsci.2011.09.012
Yuan, M., Diller, T. T., Bourell, D., & Beaman, J. (2013). Thermal conductivity of polyamide 12 powder for use in laser sintering. *Rapid Prototyping Journal*. https://doi.org/10.1108/RPJ-11-2011-0123
Zäh, M. F., & Lutzmann, S. (2010). Modelling and simulation of electron beam melting. *Production Engineering*. https://doi.org/10.1007/s11740-009-0197-6
Zhang, D. Q., Cai, Q. Z., Liu, J. H., Zhang, L., & Li, R. D. (2010). Select laser melting of W-Ni-Fe powders: Simulation and experimental study. *International Journal of Advanced Manufacturing Technology*. https://doi.org/10.1007/s00170-010-2641-3
Zhang, T., & Kang, H. J. (2021). Enhancement of the processability and properties of nylon 6 by blending with polyketone. *Polymers*, *13*(19). https://doi.org/10.3390/polym13193403
Zhou, W. Y., Lee, S. H., Wang, M., Cheung, W. L., & Ip, W. Y. (2008). Selective laser sintering of porous tissue engineering scaffolds from poly(L-lactide)/carbonated hydroxyapatite nanocomposite microspheres. *Journal of Materials Science: Materials in Medicine*, *19*(7), 2535–2540. https://doi.org/10.1007/s10856-007-3089-3

Appendix A

Comsol model data

Sample Input parameters for PA6CB

Name	Expression	Value	Description
x0	0[mm]	0 m	origin x
y0	0[mm]	0 m	origin y
sigx	0.1[mm]	1E-4 m	dia of beam
sigy	0.1[mm]	1E-4 m	dia of beam
Q	1[W]	1 W	Laser power
Rc	0.05	0.05	Reflectivity
Ac	0.95[1/cm]	95 1/m	Absortptivity
T_trans	475[K]	475 K	phase change temp
dT	01[K]	1 K	transition interval
lf	190000[J/kg]	1.9E5 J/kg	Latent heat of fusion
rho_melt	2000[kg/m^3]	2000 kg/m³	melt density

Heat transfer model with phase change and boundary conditions

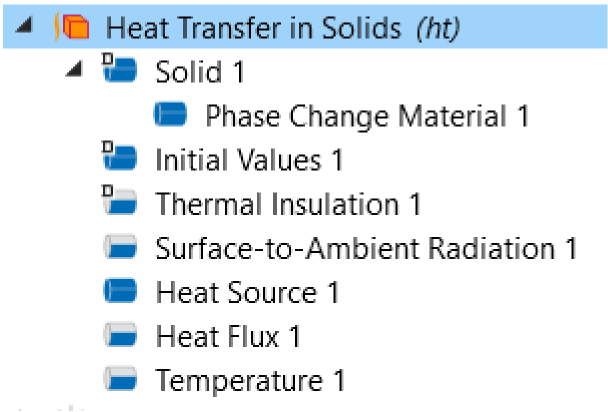

Appendix B

Visual Basic Code for converting SEEK camera raw image to temperature data

```
Sub txt2csv()
    Dim Fname As String, ipath As String, retstring, fs, a ', i As Long
    Dim i As Integer, j As Integer
    Dim lngTemp As Long

    Dim varArrayLines As Variant
    Dim varArrayValues As Variant
    Dim wbkWorkbook As Workbook

    With Application.FileDialog(msoFileDialogFolderPicker)
        .AllowMultiSelect = False
        If .Show = -1 Then ipath = .SelectedItems(1) Else Exit Sub
    End With
```

```
Application.ScreenUpdating = False
On Error Resume Next

Fname = Dir(ipath & "\*.txt")

Do While Fname <> ""
    Set fs = CreateObject("Scripting.FileSystemObject")
    Set a = fs.OpenTextFile(ipath & "\" & Fname, 1, 0)

    retstring = a.readall

    a.Close 'Close file

    'Remove brackets
    retstring = Replace(retstring, "[", "")
    retstring = Replace(retstring, "]", "")

    If Err.Number = 0 Then

        'Store all lines to array. ; marks the end of line
        varArrayLines = Split(retstring, ";")

        retstring = vbNullString 'Make retstring empty

        For i = 0 To UBound(varArrayLines)

            'Debug.Print varArrayLines(i)
            'Split each line into values (separated by ,)
```

```
                varArrayValues = Split(varArrayLines(i), ",")

                'Apply formula to each value.
                For j = 0 To UBound(varArrayValues)
                    varArrayValues(j) = Round((0.0397 * varArrayValues(j)) - 587.25, 2) + 5
                    'T = (0.0457X)-687.26,, 0.0397x - 587.25
                Next j

                retstring = retstring & WorksheetFunction.TextJoin(",", False, varArrayValues) & "," & Fname & vbCrLf 'Write line in text file

            Next i

            'Remove vbcrlf from the end
            retstring = Left(retstring, Len(retstring) - 2)

'           'Add filename at the end
'           retstring = retstring & "," & Fname

            'Write to text file.
            Open ipath & "\" & Fname For Output As #1 'Open text file
            Print #1, retstring
            Close #1

            'Rename to CSV
            Name ipath & "\" & Fname As ipath & "\" & Replace(Fname, "txt", "csv")
        Else
```

```
        Err.Clear
      End If
      Fname = Dir
    Loop

    Set fs = Nothing: Application.ScreenUpdating = False

End Sub
```